UNIVERSITY OF CALIFORNIA SAN DIEGO

Water in the Deep Continental Crust Through a Comparison of Xenoliths and Paleo-Arc Terranes

A Thesis submitted in partial satisfaction of the requirements
for the degree Master of Science

in

Earth Sciences

by

Sean Curran

Committee in charge:

Professor Emily Van Allen, Chair
Professor Jeffrey Gee
Professor Richard Norris

2023

The Thesis of Sean Curran is approved, and it is acceptable in quality and form for publication on microfilm and electronically.

University of California San Diego

2023

Table of Contents

List of Supplemental Files

curran_famatinia_eds.zip

curran_stateline_eds.zip

curran_thinsections_scans.zip

curran_stateline_pyroxene_grainsize.xlsx

curran_tables.xlsx

List of Figures

List of Tables

Abstract of the Thesis

Water in the Deep Continental Crust Through a Comparison of Xenoliths and Paleo-Arc Terranes

by

Sean Curran

Master of Science in Earth Sciences

University of California San Diego, 2023

Professor Emily Van Allen, Chair

Multiple models exist for forming continental crust (e.g. mantle plumes, relamination, arc magmatism), each with different implications for water budget and distribution. Arc systems produce garnet-pyroxene rich rocks within lower crust and these are generally defined as eclogite (metamorphosed basalt) or arclogite (igneous cumulate). The former should be dehydrated and the latter hydrated. By quantifying water content and trace elements of nominally anhydrous

minerals (NAMs) from lower crustal rocks we may assess the mode of their formation. Analyses of Proterozoic, kimberlite-hosted two-pyroxene garnet granulite xenoliths from State Line, CO suggest an igneous origin. Using energy dispersive spectroscopy (EDS) maps and average mineral water contents, we find that whole rocks contain 100 to 650 ppm H_2O, with clinopyroxene as the main water-bearing NAM. Analyses of Paleozoic amphibole gabbronorites from the exhumed Famatinia Arc, Argentina indicate secondary mineralization of hydrous phases with amphibole being the primary carrier for water. Additionally, comparison of observed trace element partitioning between NAMs in xenoliths shows that 1) reconstructed bulk rocks can "see through" the host magma contamination, but 2) care must be taken to account for accessory minerals, which may incorporate significant trace elements, in reconstructing bulk compositions. Comparison of xenolith vs. exhumed arc lower crust suggests that the latter may experience retrogression and re-equilibration of NAM water content, resulting in re-partitioning that is not representative of the original hydration state at depth.

Introduction

Since at least 3.0 Ga, subduction processes have been essential in the formation of calc-alkaline rocks and associated continental crust (Arndt, 2013). As a result of subduction, the lower continental crust is composed of two primary igneous mafic protoliths. These protoliths are 1) eclogite, defined as metamorphosed tholeiitic basalt formed by subducting oceanic crust (Defant and Drummond, 1990), subducting oceanic terranes (Cavosie and Selverstone, 2003; Scholl et al., 1986), and mafic underplating through accretion of oceanic plateaus (Condie, 1999), and 2) arclogite (Lee and Anderson, 2015), pyroxene and garnet-rich cumulates generated through fractionation of primitive hydrous basaltic arc magmas (Ducea, 2002; Lee, 2014). These mafic lower crustal components yield silica-rich magmas when partially melted, leaving behind a high density restite that may be susceptible to foundering or delamination from the more buoyant upper crust. The siliceous component derived from this partial melting is generally preserved in the crust owing to its low density, though it is unknown how much is formed from either eclogite (Rapp et al., 2003) or arclogite (Jagoutz, 2010; Lee et al., 2006).

Magmatic water content is a principal discriminating factor in determining petrogenesis through tholeiitic or calc-alkaline trends (Sobolev and Chaussidon, 1996). Eclogitic protoliths are relatively water-poor due to dehydration through prograde metamorphism, and derivative melts in equilibrium with eclogitic residues reflect these anhydrous conditions. High temperature igneous arclogites should, in theory, reflect equilibrium with more hydrous melts since calc-alkaline magma water contents are ~2 wt. % at a minimum (Plank et al., 2013). Further fractional crystallization evolves more hydrous derivative melts which have been shown to fractionate garnet-pyroxene rich cumulates in the lower crust (Lee et al., 2006; Müntener and Ulmer, 2006), and amphibole-rich cumulates within the middle crust (Davidson et al., 2007). The budget for

magmatic water in the deep crust has an important influence on petrophysical properties such as cumulate mineralogy, lower crustal rheology, and bulk crustal composition. High magmatic water content expands the liquidus field of pyroxene over plagioclase (H. S. Yoder and Kushiro, 1969) resulting in pyroxenes dominating the mineralogy of lower continental crust compared to the abundance of plagioclase cumulates in oceanic lower crust (Chin et al., 2018). Water also plays a crucial role in crustal melting processes (Collins et al., 2020) because water lowers the solidus. Furthermore, even at parts per million (ppm) levels, increasing water content within mineral lattices influences important physical properties such as enhancing crystal plasticity and reducing rock viscosity (Hirth and Kohlstedt, 1995). In context of garnet-pyroxene rich lower crustal rocks these factors represent important controls on the susceptibility for foundering or delamination of dense, mafic arc crust and preservation of derivative, buoyant, felsic continental crust.

Water contents of primary magmas can be difficult to establish considering the limitations on direct sampling of these magmas. Early formed phenocrysts or cumulates, if not rehydrated (or degassed) during exhumation, may preserve water contents of melts last in equilibrium and provide the best opportunity to determine these values. We use this approach to probe the hydration state of stable lower continental crust and infer water content of magmas that fractionated in the crust. We report water content analyzed by secondary ion mass spectrometry (SIMS) in nominally anhydrous minerals (NAMs) of two crustal suites; granulite xenoliths of Proterozoic age from the State Line kimberlite district, Northern Colorado, USA and Ordovician mafic-ultramafic arc cumulates from the exposed paleo-arc section of the Sierra de Valle Fertil, Argentina**.** In addition, we present new mineral trace element data on State Line xenoliths. Trace elements are important fingerprints of petrogenetic processes, and we couple the trace element

data to our NAM H_2O dataset to better assess the petrogenetic history of the State Line xenoliths. Using averaged mineral H_2O and trace element concentrations, combined with mineral modes acquired from EDS compositional maps, we were able to reconstruct the bulk rock concentrations of these elements. Bulk rock water concentrations provide an estimate of the water budget in the lower crust.

One goal of this thesis is to evaluate whether major differences in NAM H_2O contents exist across different subduction zones and different exhumation styles. To these ends, the State Line and Famatinia localities provide important contrasts and similarities. The Famatinia arc contains one of few continuous deep arc crust exposures worldwide with minimal deformation, making it an excellent setting for investigating the petrology and geochemistry of lower continental crust. The age of formation and eruption for State Line xenoliths make them ideal for constraining water content of stable lower continental crust. The deep lithosphere of this region contains rocks of Paleoproterozoic age, eruption of these xenoliths in the Devonian predates the Laramide orogeny which is thought to have caused extensive hydrous overprinting within the deep lithosphere through metasomatism associated with flat slab subduction beneath southwestern North America (Jones et al., 2015; Li et al., 2008)**.** This study is motivated by comparing the hydration state of NAMs between these localities with shared petrogenetic arc origins yet differing exhumation histories. The State Line samples, being undisturbed from Proterozoic formation through its eruption in Devonian functions as a baseline for stable arc derived lower crust while the Famatinia sample suite represent a tectonically exhumed arc.

Geologic Background

State Line Kimberlite District, Colorado, USA

The State Line Kimberlite District constitutes ~40 hypabyssal to diatreme-facies kimberlite exposures containing deep lithosphere xenoliths of crustal and mantle origin (Eggler et al., 1987). The diatremes were emplaced within Proterozoic continental crust of the Colorado Province (Bickford et al., 1986), near the southern edge of the Archaean Wyoming Craton. The Wyoming Craton, Medicine Hat Block, and Superior Craton amalgamated into the cratonic core of Laurentia via the Trans-Hudson orogen concluding at ~1.8 Ga (Whitmeyer and Karlstrom, 2007). A series of oceanic terranes and island arcs – namely the Yavapai Province (1.7-1.8 Ga), Mazatzal Province (1.6-1.7 Ga) and Granite-Rhyolite Province (1.35-1.55 Ga) – subsequently collided and imbricated along the southern margin of Laurentia forming large-scale northeast trending juvenile crustal belts with ages decreasing away from the cratonic core (Whitmeyer and Karlstrom, 2007). The southern growth of the Laurentia Craton ultimately ceased at ~1.0 Ga with the Grenville Orogeny, marking the end of Laurentia's long-lived convergent and/or transpressive southern plate margin (Whitmeyer and Karlstrom, 2007).

The Colorado Province remained tectonically inactive after ~1.0 Ga, experiencing virtually no significant magmatism or deformation until the end of the Paleozoic. The southern Laurentian margin then interacted with Gondwanan terranes during the Ouachita orogeny in association with the formation of Pangaea, forming the Ancestral Rocky Mountains (Keller et al., 2005). The Colorado Plateau region experienced another lull in tectonic activity which terminated at ~70 Ma with the Laramide Orogeny (Dickinson and Snyder, 1978).

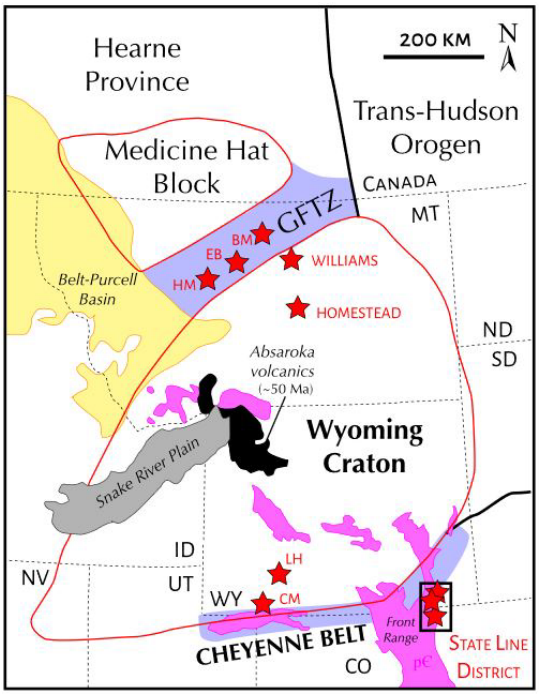

Figure 1 – State Line geologic and tectonic setting map showing key geologic features. Xenolith localities denoted by red stars. BM = Bearpaw Mountains, EB = Eagle Butte, HM = Highwood Mountains, CM = Cedar Mountains, LH = Leucite Hills, GFTZ = Great Falls tectonic zone. Pink regions denote exposed Precambrian rock. Modified from (Chin et al., 2020).

The Laramide Orogeny is characterized by low-angle flat slab subduction of the Farallon plate beneath the western North American margin initiating crustal shortening and associated structural deformation in the shallow lithosphere through thrust faulting and folding (Dickinson and Snyder, 1978). The low-angle subduction induced only minor magmatism, though significant hydration of deep lithosphere through fluid metasomatism occurred across much of the western United States (Humphreys et al., 2003). Evidence of metasomatism in the lower crust can be inferred from biotite and amphibole containing xenoliths from the Leucite Hills volcanic field (Lange et al., 2000) northwest of the Devonian-age State Line kimberlites. Additionally, distinctive geochemical signatures expressed in Cenozoic lavas found within the American Southwest region are attributed to melting of hydrous metasomatized continental lithosphere (Farmer et al., 2020).

State Line kimberlite xenoliths do not show evidence for hydrous metasomatism (Farmer et al., 2005). Lower crustal xenoliths from the State Line district include a variety of mafic lithologies but are dominated by (nominally anhydrous) mafic granulites, with subordinate amphibolite, anorthosite, and gabbroic xenoliths (Bradley and McCallum, 1984; Farmer et al., 2005). Eruption ages in the Devonian mean these rocks would have escaped any hydrous overprinting from the Laramide Orogeny. State Line kimberlite xenoliths therefore provide a rare opportunity to evaluate the water content of lower continental crust preserved since genesis.

Famatinia Arc, Argentina

The Famatinia Arc is a mid-Ordovician to Devonian age subduction complex formed along the proto-Andean margin of Western Gondwana (Cawood, 2005). The arc extends approximately 2500 km within the active foreland and along strike of the central Andes, from northern Peru to Central Argentina between latitudes 24° and 39°S. The Famatinia arc initiated at ~495 Ma and was predominantly constructed during the Early Ordovician (Ducea et al., 2010; Pankhurst et al., 1998) remaining active until ~440 Ma (Collo et al., 2009). Differential exhumation of the arc initiated during a Middle Paleozoic collisional orogen (Astini and Dávila, 2004). Exposures within the Famatinia arc include volcaniclastic rocks, calc-alkaline volcanics, gabbroic mafic rocks, and S-type plutonic rocks (Walker et al., 2015).

The Sierras de Valle Fértil (SVF) is part of the Famatinia subduction complex in northwestern Argentina and is one of few tilted sections of relatively continuous, mid to deep arc crust exposures found worldwide. The Sierras de Valle Fértil is located within the southern Famatinia belt and exposes eastward-tilted, compositionally stratified igneous arc crust with metasedimentary host-rocks at paleodepths of ~12-32 km (Otamendi et al., 2009; Tibaldi et al., 2013). Exposures of the shallowest paleodepths include nested tonalite-granodiorite plutons

which transition to heterogenous tonalite bodies, and further progression to dominantly gabbroic and tonalitic rocks at depth.

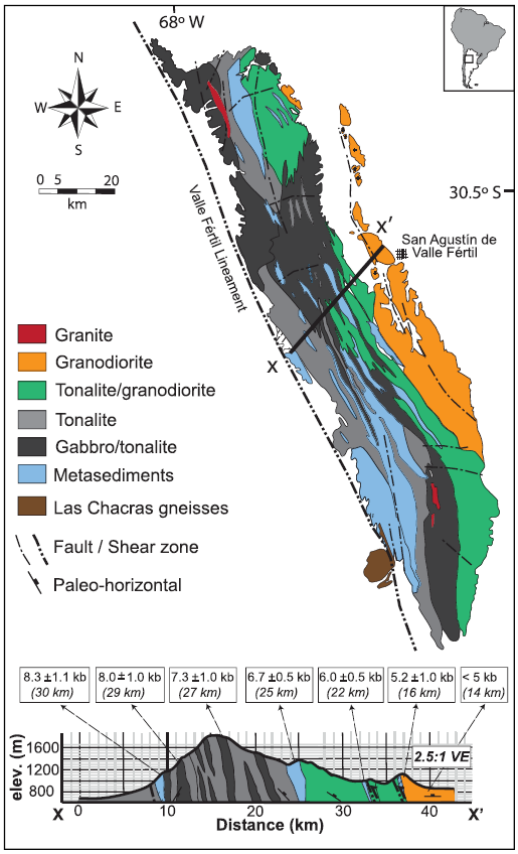

Figure 2 - Map of Sierra Valle Fertil sourced from (Walker et al., 2015) and modified from the maps of Mirre´ (1976), Vujovich et al. (1996), Otamendi et al. (2009b) and Tibaldi et al. (2013). Cross-section and barometery modified from Tibaldi et al. (2013)

This study focuses on mafic sections of the Sierras de Valle Fértil which represent the deepest exposures- rocks within this zone are dominated by tonalite, gabbronorite, norite and small ultramafic bodies. More specifically, samples included in this study were collected within sections consisting of hornblende gabbronorites and ultramafic bodies comprised of troctolite and amphibole-olivine websterite. The Sierras de Valle Fértil being one of few continuous deep arc crust exposures worldwide with minimal deformation makes it an excellent setting for investigating the petrology and geochemistry of lower continental crust.

U-Pb zircon crystallization ages from magmatic rocks show that this section of the arc was formed during a short interval in the Ordovician, from 485 to 465 Ma (Ducea et al., 2010). Age constraints on the samples can be further refined through consideration of high precision U-Pb CA-TIMS zircon data reported by (Ducea et al., 2017) yielding an approximate age of 470 Ma. The data reported by Ducea et al. (2017) analyzed samples collected within a few kilometers of the samples considered in this study. These ages are interpreted to be metamorphic ages and are consistent with previously published zircon U-Pb ages on metasedimentary rocks (Ducea et al., 2017).

Methods

We use secondary ion mass spectrometry (SIMS) to quantify water content in nominally anhydrous minerals. We also use laser ablation inductively coupled plasma mass spectrometry to measure trace element concentrations in these minerals. Mineral modes are determined through pixel counting of energy dispersive spectroscopy (EDS) maps and used in conjunction with SIMS and inductively coupled mass spectrometery (ICPMS) data to reconstruct whole rock water and trace element compositions.

EDS Maps and Pixel Counting

Energy dispersive spectroscopy (EDS) maps were obtained for selected thin sections using an FEI Apreo LoVac field emission gun scanning electron microscope (SEM) at UC San Diego. Operating parameters were an accelerating voltage of 20kV, beam current of 3.2 nA, 10 mm working distance, and 250 to 800 µs dwell time with a 512x512 resolution**.** Increased dwell time resulted in higher contrast between mineral phases and was maximized in accordance with available session length. Some samples were analyzed with a 25 nm gold coat which, while not necessary, tended to produce higher quality data.

Mineral modal percentages were determined by pixel counting with Adobe Photoshop. The following image types were utilized: a) EDS maps collected on an FEI Apreo LoVac SEM at 3.2 nA and 20 kv, 512x512 resolution and a dwell time of 250-800 µs, b) Light microscopy images comprising either whole thin section scans (scanned under plane-polarized and cross-polarized light with a Nikon SuperCoolScan 9000 ED 35 mm film scanner), and c) composite reflected light images taken using an Olympus petrographic microscope.

Prior to pixel counting, all images were edited to remove pixels which represent thin section glass, epoxy, and/or Suprasil standard. EDS images were then either counted directly in Photoshop or slightly modified through levels adjustment to enhance the range of color values present, thus creating more discrete color values for each mineral. RGB stacks were then constructed using ImageJ. RGB stacks used for pixel counting consisted of three major element EDS maps. The elements selected per stack were chosen based on the sample mineral assemblage. In some cases, mineral compositions were too similar to create discrete color values for each mineral in a stack and a thin section scan or reflected light image was used as a check for phase identification.

Pixel counting with Adobe Photoshop utilizes the built-in Magic Wand Tool to count the number of pixels for a particular color value. Using the Magic Wand Tool, the number of pixels representative of each mineral in a given sample was determined. Pixel counting was performed using the Point Sample selection option and a tolerance of 1-3. These settings were fine-tuned to increase precision and avoid inadvertent selection of extraneous pixels. In some cases where mineral color values were substantially different from the rest of the minerals present, a 3x3 average pixel selection was used. The total number of pixels counted was summed and compared to the total pixels in the countable region. These pixel counts were determined using the

Histogram tool. To calculate modes, the number of pixels counted for a mineral were divided by the total number of pixels counted for the sample.

LA-ICPMS

Laser Ablation Inductively Coupled Plasma Mass Spectrometry (LA-ICPMS) analyses were performed at Scripps Isotope Geochemistry lab of Scripps Institution of Oceanography with the guidance of Prof. James Day and lab members. High resolution reflected light photographs were used to determine the location of previous SIMS data measurements where LA-ICPMS data were to be collected within the same grains whenever possible.

Pre-selected spot locations were measured with a New Wave Research (NWR) UP213 Laser Ablation System coupled to a Thermo Fisher Scientific™ iCAP™ WC ICP-MS instrument. A standard laser spot size of 100 micrometers, with a 5 Hz repetition rate was used. Laser output percentage was set to 43% with fluence ranging from 2.95 to 3.3 J/cm^2. Reference standards were measured within the same session, each standard being measured at least twice before and after the sample were analyzed. Standards chosen were NIST 610, NIST 612, BHVO-2g, BIR-1g, BCR-2g, all commonly used in analyzing silicate minerals for their homogeneity and range of trace-element compositions at consistent values. Additionally, NIST 610 and BHVO-2g were measured halfway through the session to assess any drift in sensitivity during the analyses of which no significant drift was detected. The isotopes measured include: ^{7}Li, ^{24}Mg, ^{27}Al, ^{29}Si, ^{39}K, ^{44}Ca, ^{45}Sc, ^{48}Ti, ^{51}V, ^{52}Cr, ^{55}Mn, ^{57}Fe, ^{59}Co, ^{60}Ni, ^{85}Rb, ^{88}Sr, ^{89}Y, ^{90}Zr, ^{93}Nb, ^{133}Cs, ^{137}Ba, ^{139}La, ^{140}Ce, ^{141}Pr, ^{146}Nd, ^{147}Sm, ^{153}Eu, ^{157}Gd, ^{159}Tb, ^{163}Dy, ^{165}Ho, ^{166}Er, ^{169}Tm, ^{172}Yb, ^{175}Lu, ^{178}Hf, ^{181}Ta, ^{208}Pb, ^{232}Th, ^{238}U.

Individual spot measurements were taken over an 83 second period. Background measurements were taken the first 23 seconds while the laser was firing without sample ablation. After 23 seconds the laser shutter was opened allowing sample ablation over a period of 60 seconds. Stability of measured intensities in counts per second (cps) during background measurement and sample ablation was considered for each individual measurement taken, with the 0-20 second interval of analysis used as background and 30-83 second interval used as the sample measurement. LA-ICP-MS data were reduced using the LasyBoy v3.5 MS Excel macro developed by Joel Sparks at Boston University. Normalizing isotopes were ^{44}Ca for all calcium bearing minerals and ^{24}Mg for calcium devoid silicates such as orthopyroxene. Calcium and Magnesium concentrations for normalization were obtained through EMP at Brown University as previously mentioned.

Electron Microprobe Analysis (EMP)

Major element composition of pyroxenes, garnet, plagioclase, amphibole, and phlogopite were analyzed by electron microprobe using a CAMECA SX100 at Brown University (accelerating voltage 15kV, beam current 20nA, spot size 1 micrometer). In-house mineral standards and secondary mineral standards were used for calibration. Relative standard deviation was <1% for major elements and ~5% for minor elements. Major element compositions from EMP are used as internal standard for trace element data reduction.

Secondary Ion Mass Spectrometry (SIMS)

H_2O of nominally anhydrous minerals was measured by ion microprobe *in situ* in petrographic thin sections. New one inch round thin sections were made from previously collected material. Prior to thin section preparation, each billet was microdrilled and a grain of commercially available Suprasil glass (H_2O content 1 ppm; certified by Heraeus Quarzglas was

embedded in the center of the xenolith, ensuring a flush and well-polished surface. The purpose of the Suprasil glass is to monitor the instrumental H_2O background, a critical factor due to the ubiquitous presence of volatile-rich epoxy in petrographic thin sections and the typically low H_2O concentrations of nominally anhydrous minerals.

To minimize background H_2O, prior to analysis the ion microprobe was baked for ~2 days to reach ultrahigh vacuum of ~$2x10^{-10}$ torr. During an analytical session, four thin sections, plus a separate block with mineral standards, were simultaneously introduced into the airlock at ~$5x10^{-9}$ torr for at least 4 days, in some cases up to 7 days, to ensure complete degassing of extraneous H_2O from the sample epoxy. Analyses were obtained using a CAMECA 7f-Geo SIMS, using following operation parameters: primary Cs+ beam with current of 4.5-5nA, accelerating voltage of 10kV, rastered over a 20x20 micrometer area with a field aperture limiting the secondary ion collection area to an 8 micrometer spot in the center of the rastered area. Each analysis comprised 2 min of presputtering then 30 cycles through the mass sequence ^{12}C, $^{16}O^{1}H$, ^{18}O, ^{19}F, ^{27}Al, Cl, and ^{30}Si. OH (or H_2O) was determined by using a mass resolving power of ~5200 to separate $^{16}O^{1}H$ from ^{17}O; H_2O concentrations were determined using calibration curves (supporting information [SI] Figures S1-S6 of (Chin et al., 2020) developed using mineral standards from Aubaud et al. (2007), Mosenfelder et al. (2011), and Mosenfelder and Rossman (2013a, 2013b). During analyses the ion image and counts were monitored at all times, and any visible "hot spots" in the ion image (presumably corresponding to tiny, cracks, or heterogeneities) were noted and corresponding cycles deleted if necessary. ^{12}C was used as a monitor for contamination and/or cracks. Any measurements with high levels of ^{12}C, ^{19}F, or visible perturbations in the ion image were not reported.

The minerals analyzed (garnet, pyroxene, plagioclase, amphibole, apatite, and phlogopite) have a wide range of Si and so to minimize matrix effects we normalized masses to ^{18}O, since the O contents of most silicate minerals are very similar (in contrast to Si which can vary by tens of weight %). Estimation of uncertainties followed the protocol outlined in Chin et al. (2016) and ranged from 10% to 15% (2 relative standard error [RSE]). Over the course of two analytical sessions, the average H_2O background ranged between ~15 and ~30 ppm; we background corrected all analyses using an average value of 23 ppm.

Data and Results

In this section, I describe the results from EDS mapping, LA ICPMS, and SIMS. Optical petrography and EDS mapping were used together to describe the mineralogy of all samples. For the State Line xenoliths, modes derived from EDS maps of thin sections were used in conjunction with averaged trace element and water concentrations to reconstruct the bulk compositions.

Mineralogy and Petrography – EDS Maps

(Fig. 3) shows an example EDS map RGB stack which can be used for determining modal mineralogy. In this stack the RGB channels are assigned to Calcium, Aluminium, and Silica respectively.

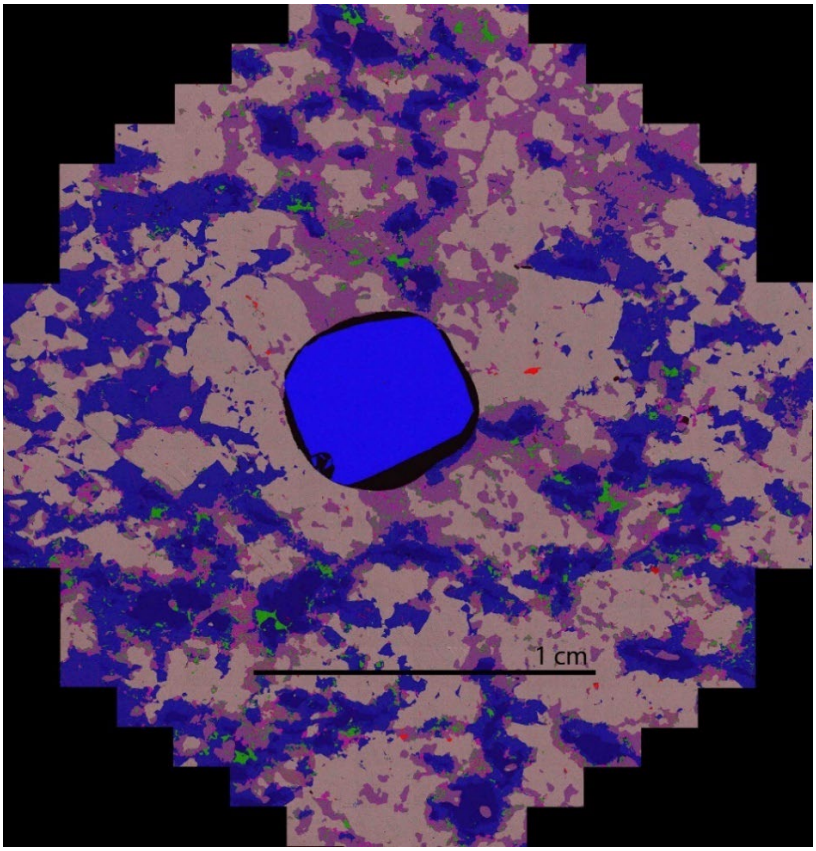

Figure 3 – Calcium(R) Aluminium(G) Silica(B) EDS map RGB Stack, Sample FA1206 amphibole websterite.

(Fig. 3) is an example of an ideal EDS map RGB stack for pixel counting. The resultant color value for each mineral is unique enough to determine modal percentage of all phases. The following table shows the minerals present, which elements they contain, and their resultant color.

Table 1 – Phase table for **(Fig. 3)** EDS RGB stack

	Calcium (Red)	Aluminium (Green)	Silica (Blue)	Resultant Color
Apatite	X			Red
Spinel		X		Green
Clinopyroxene	X	X	X	Pink
Olivine			X	Dark Blue
Orthopyroxene		X	X	Blue
Amphibole	X		X	Purple
Plagioclase	X	X	X	Beige

At full resolution these EDS images can preserve even sub-millimeter scale textures. **(Fig. 4)** shows clinopyroxene+spinel symplectite using the same Calcium, Aluminium, Silica RGB stack.

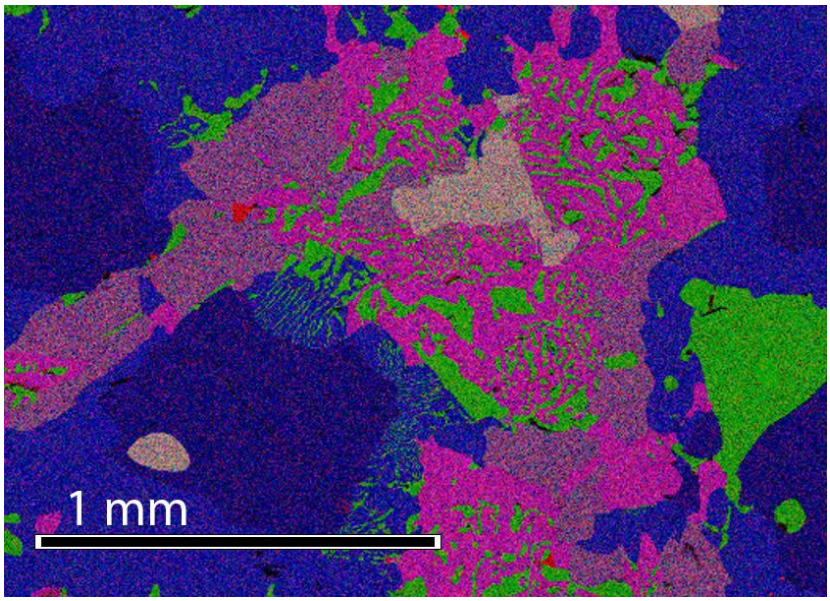

Figure 4 – Sample FA1206 EDS RGB Stack Calcium (R) Aluminium (G) Silica (B) subsection of **(Fig. 3)** showing clinoypyroxene+spinel symplectite.

Mineralogy and Petrography – State Line

Lower crustal xenoliths from the State Line district include mafic lithologies but are dominated by (nominally anhydrous) mafic granulites, with subordinate amphibolites, anorthosites, and gabbroic xenoliths (Bradley and McCallum, 1984; Farmer et al., 2005). We selected four samples from the Sloan 2 (SD2) and Schaeffer (SH) kimberlite pipes located in the Front Range in north central Colorado (Bradley and McCallum, 1984). These previous studies showed that the modal mineralogy of the State Line lower crustal xenoliths is dominated by clinopyroxene, orthopyroxene, plagioclase, and garnet; these phases constitute >90% volume of most of the xenoliths (Bradley and McCallum, 1984). Our EDS mapping confirms these previous mineral modes. Amphibole occurs in some 2-pyroxene granulites (Bradley and McCallum, 1984; Farmer et al., 2005) but is absent or rare in the garnet-bearing xenoliths. The most common accessory minerals amongst the State Line samples are ilmenite, rutile, and apatite. Farmer et al. (2005) also reported minor amounts of zircon, barite, and K-Feldspar. The latter two minerals were interpreted as grain boundary contaminants from the host kimberlite as observed in K-rich phases along grain boundaries and K-feldspar occasionally replacing plagioclase grains.

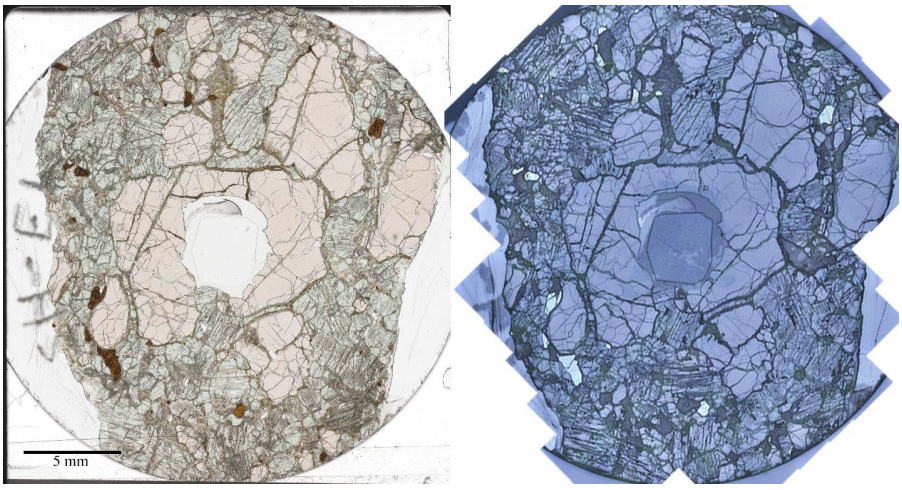

Figure 5 - SH-E1: arclogite, plane polarized light thin section scan (left) and composite reflected light image (right).

SH-E1: Arclogite, very coarse grained (>1cm) and composed of approximately equal proportions of Garnet (49%) and Clinopyroxene (51%), with minor rutile. Classified as an eclogite by Farmer et al., 2005. Garnet grains are very large (1-3 cm) with irregular, interlobate grain boundaries with clinopyroxene embayments. Rutile occurs as 0.15 to 1.5 mm grains with euhedral to rounded expression.

SD2-L110: two-pyroxene granulite; medium-grained subhedral granoblastic with 40% clinopyroxene, 40% garnet, 15% orthopyroxene, ~4% plagioclase + K-spar, ~1% apatite, with minor ilmenite, phlogopite, and hornblende. Clinopyroxene occurs as 0.8 to 2.1 mm anhedral to subhedral grains, largest grains occasionally forming equant bands with oxide intergrowths. Apatite is disseminated but less common in clinopyroxene bands and occurs as 0.05 to 0.2 mm rounded grains. Garnet grains are anhedral 0.3 to 2.3 mm with undulating grain boundaries, garnet-clinopyroxene coronas are small and uncommon. Plagioclase occurs interstitially between garnet and clinopyroxene as subhedral to anhedral fine to medium <1.5 mm grains.

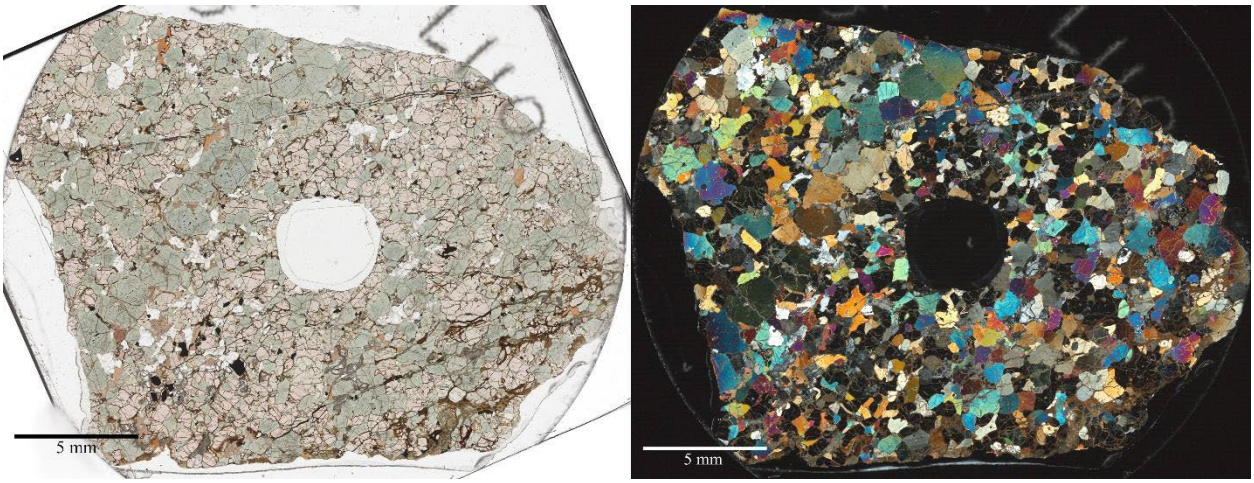

Figure 6 - SD2-L110: two-pyroxene granulite, plane polarized thin section scan (left) and cross polarized (right).

SD2-LC71: two-pyroxene granulite; medium- to coarse-grained granoblastic with 35% clinopyroxene, 29% garnet, 23% plagioclase, 12% orthopyroxene, minor ilmenite, and trace K-spar. A distinctive feature is the prevalent garnet-clinopyroxene coronas which comprise up to 30% or more of the sample. Farmer et al. (2005) noted the abundance of garnet-clinopyroxene coronas in several State Line granulite xenoliths and interpreted the coronas to form from pre-existing orthopyroxene and calcic plagioclase. Within coronas, clinopyroxene occurs as small, worm-like grains surrounded by garnet; outside coronas, clinopyroxene occurs either as 0.05 to 0.2 mm rims around orthopyroxene or as large 1.2 to 6mm porphyroclasts. In all cases the coronae are observed to form adjacent to plagioclase grains which range in size from ~1.0 to 4.6 mm. Ilmenite grains have undulating grain boundaries with grain sizes ranging from 0.2 to 1 mm and generally occur adjacent to garnet, though some grains are observed to be isolated by plagioclase or clinopyroxene. A few dilation fractures with localized alteration propagate across the entire length of the sample, while smaller fractures that propagate across grain boundaries without offset are common and most abundant in coarse plagioclase and clinopyroxene porphyroclasts.

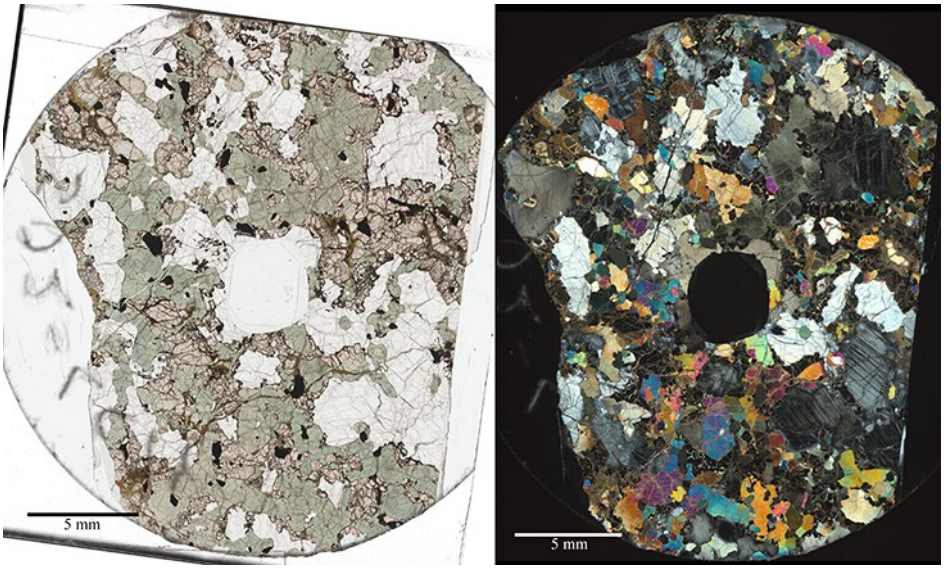

Figure 7 - SD2-LC71: two-pyroxene granulite, plane polarized thin section scan (left) and cross polarized (right).

SD2-LC120: two-pyroxene granulite; medium- to coarse-grained, contains 10% clinopyroxene, 30% orthopyroxene, 25% garnet, 35% plagioclase, with minor ilmenite, K-spar, and trace rutile/zircon. Medium to coarse grain anhedral orthopyroxene and plagioclase with interstitial clinopyroxene, ilmenite, and rutile. Garnet occurs throughout in fine-grained clusters and in weakly developed coronas around orthopyroxene. Rutile occurs as subrounded medium size grains.

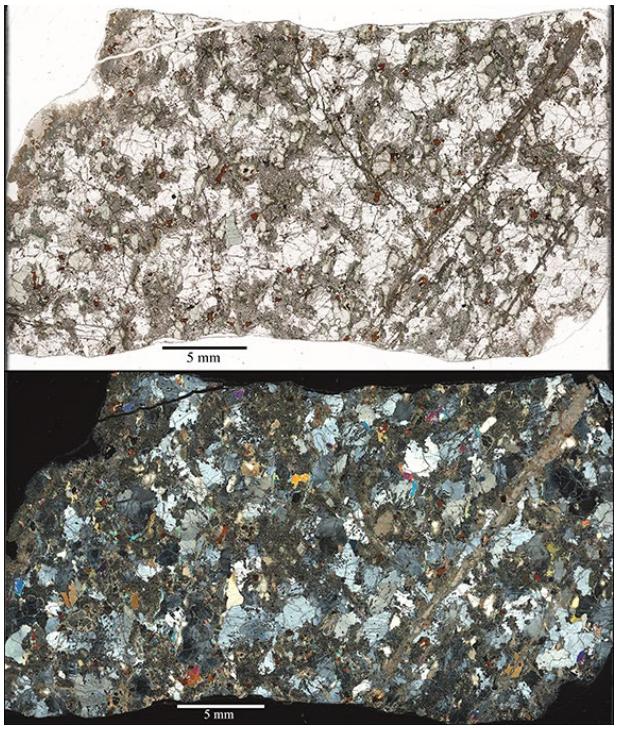

Figure 8 - SD2-LC120: two-pyroxene granulite, plane polarized thin section scan (top) and cross polarized (bottom).

Mineralogy And Petrography - Famatinia

Samples selected for this study from the Famatinia arc include a variety of mafic lithologies but are dominated by amphibole and plagioclase rich cumulates. We analyzed four samples from the Usno, Turbante, and Algarrobo canyons located in the SVF. The SVF terrane local to the samples is dominated by tonalite and gabbronorite lithologic units, with minor exposures of ultramafic cumulates, fine-grained mafic dikes, and small felsic intrusions (Walker et al., 2015). Meta-sedimentary host rock is also present though this study will focus solely on

the mafic cumulates. The mode of the tonalites is plagioclase dominant, with variable percentages of quartz, orthopyroxene, amphibole, biotite, and Fe-Ti oxides. Tonalite grain size varies from medium to coarse (<1cm). Gabbronorite typically exhibits medium size grains (<0.5 cm) with plagioclase being modally dominant and containing variable amounts of pyroxene, amphibole, and quartz. Gabbronorites also contain zircon, apatite, pyrite, and spinel in trace volumes (Walker et al., 2015).

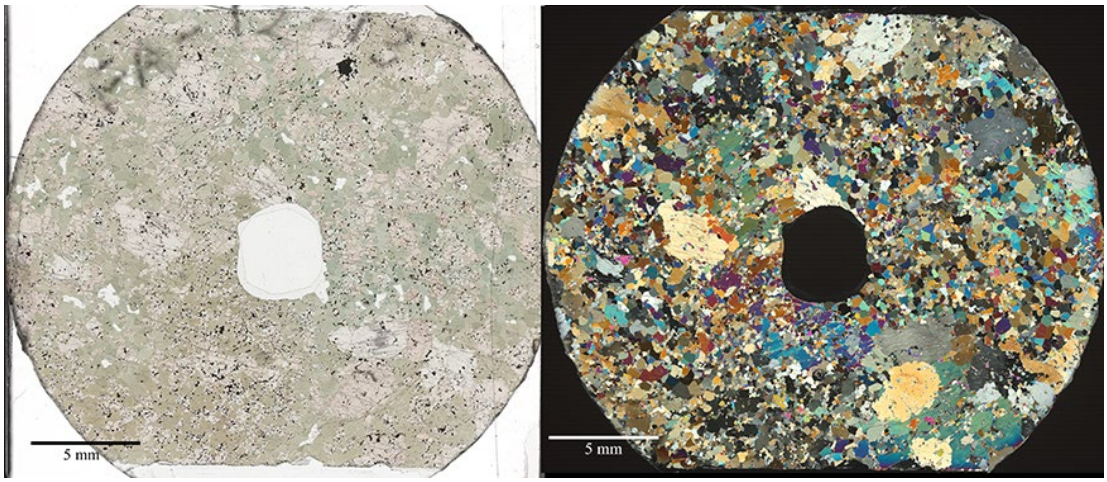

Figure 9 - FA-12-13: amphibole-olivine websterite, plane polarized thin section scan (left) and cross polarized (right)

FA-12-13: Amphibole-Olivine Websterite, contains 40.6% amphibole with clinopyroxene, orthopyroxene, plagioclase, olivine, and oxides. This sample exhibits inequigranular grain size distribution and hypidiomorphic-granular grain shape **(Fig. 9)**. Grain relations are primarily granoblastic. Orthopyroxene grains are observed in two grain size populations, with larger anhedral grains exhibiting exsolution lamellae. Large amphibole grains are poikilitic, containing orthopyroxene and clinopyroxene chadacrysts. Additionally, the population of large amphibole grains are seen to be optically continuous and anhedral while the smaller amphibole grains are subhedral with mosaic triple junction grain boundaries. The largest orthopyroxene and amphibole grains constitute a band across the sample which is slightly askew to the primary fracture orientation. These fractures are oriented in a largely unidirectional

distribution and propagate across grain boundaries. Ubiquitous anhedral magnetite exists along grain boundaries within amphibole and orthopyroxene oikocrysts.

FA-09-18: Quartz-Norite, contains 71.3% plagioclase, 16.9% orthopyroxene, 2.9% biotite/phlogopite, 3.8% quartz, 1.1% K-feldspar, 1.5% hornblende, 1.2% Fe oxide, 0.5% ilmenite (modal values previously measured). Pyroxene grains are 0.1 to 0.5 mm, subhedral, highly fractured and form aggregates. Mica are randomly oriented 0.4 to 2 mm anhedral grains and do not display fractures or deformation that are seen in other silicate phases. Plagioclase grains range from sub mm to 5 mm grains which exhibit irregular, interlobate grain boundaries. Oxide grains vary in size with the largest being ~1 mm, distribution of oxide grains is generally proximal to pyroxene aggregates and micas. A network of plagioclase extends across the sample with a subtle alignment of fracture orientation, indicating that the plagioclase may be the primary mineral accommodating deformation **(Fig. 10)**.

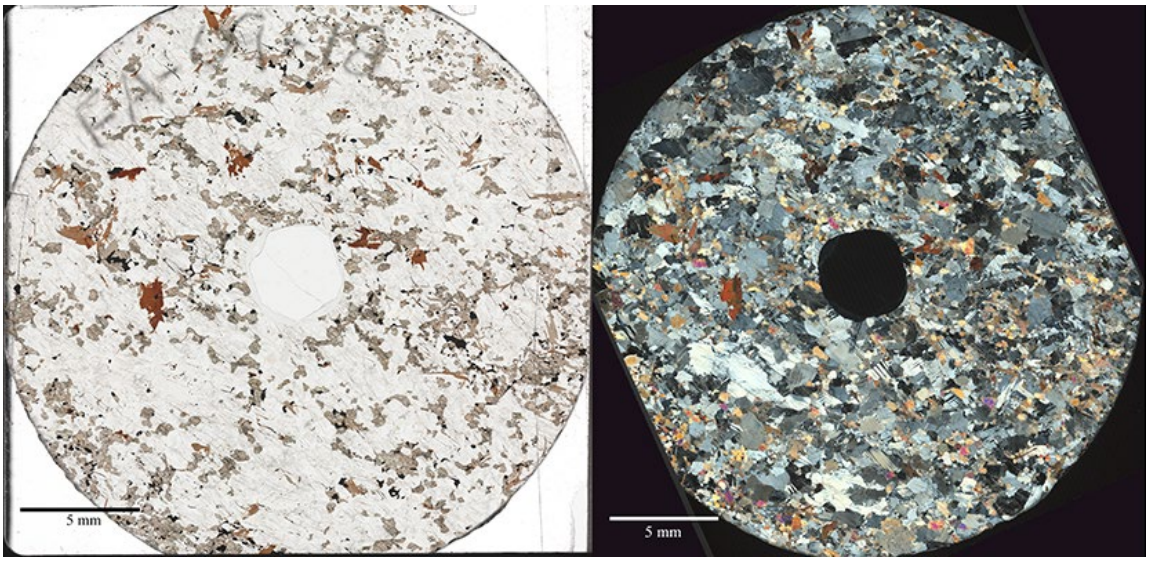

Figure 10 - FA-09-18: quartz-norite, plane polarized thin section scan (left) and cross polarized (right).

FA2-11-01B: Relict Troctolite, contains 28.9% amphibole with plagioclase, phlogopite, pyroxene. A distinctive feature of FA2-11-01B is the occurrence of amphibole coronas with

apparent relict olivine cores **(Fig. 11)**. EDS data suggests they are magnesium rich with negligible calcium and aluminium content. These altered cores are highly fractured, exhibit irregular grain boundaries and a mesh texture. SIMS analyses indicate these altered cores have been hydrated suggesting serpentinization has occurred. Altered core shape and size is observed to be consistent with relative corona shape and size in some grains. This sample is interpreted as a troctolite which has interacted with hydrous residual liquids, facilitating a reaction between olivine and plagioclase and resulting in mineralization of hornblende and phlogopite (Gallien et al., 2012). Grain relations of plagioclase and amphibole range from granoblastic interlobate to granoblastic polygonal, with larger grains exhibiting more irregular boundaries. Plagioclase grain size varies from 0.3 to 3 mm. Amphibole coronas range from thin 0.15 mm bands to larger sections ~2 mm across. Amphibole forms an optically continuous anastomosing network across large swaths of the sample, consistent with a genesis through secondary mineralization.

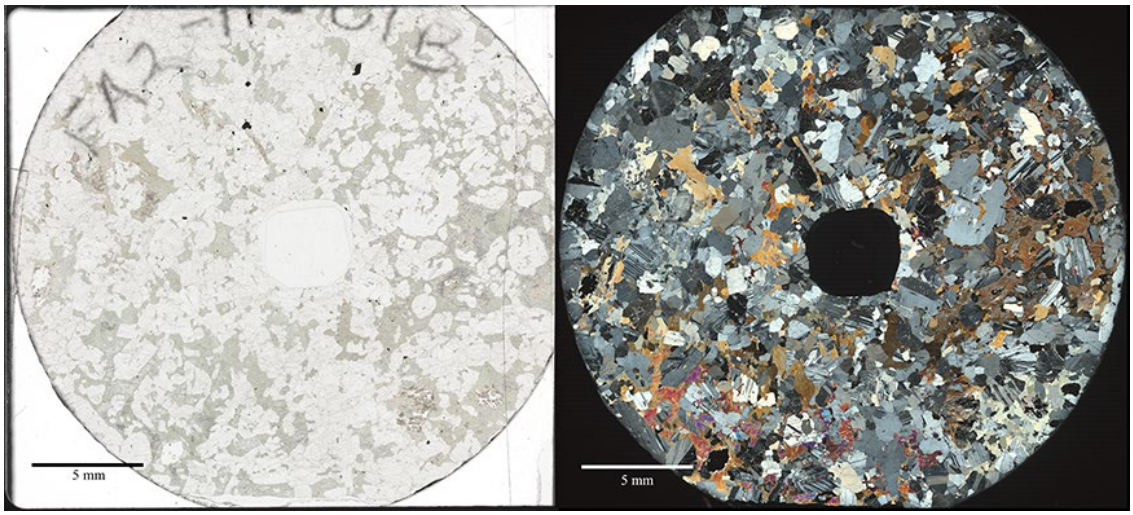

Figure 11 - FA2-11-01B: relict troctolite, plane polarized thin section scan (left) and cross polarized (right)

FA-12-06: Amphibole Websterite, contains 31.5% amphibole with plagioclase, orthopyroxene, olivine, clinopyroxene, and spinel. FA-12-06 is distinguished by its well-developed multi-layer coronas between olivine and plagioclase **(Fig. 12)**. Gallien et al. (2012)

noted the abundance of multi-layer coronas in gabbroic rocks from the Sierras de Valle Fértil region and interpreted these as reaction zones which formed at the interface between two mutually incompatible minerals during cooling at the gabbro-granulite transition. In general, the coronas are composed of an inner shell of orthopyroxene around olivine and an outer shell comprised, in most cases, of an amphibole layer followed by a clinopyroxene+spinel and/or amphibole+spinel symplectite adjacent to plagioclase. In all cases, the shape of the corona layers parallels the shape of the central olivine grain. The inner orthopyroxene shell varies in width from 0.03 to 0.30 mm with a gently undulating contact with the olivine core. The outer contact with amphibole is irregular and, in some areas, orthopyroxene does not wholly enclose the olivine and is replaced by an amphibole layer. The outer shell has a width of up to 0.80 mm with an inner layer generally comprised of inclusion free amphibole adjacent to orthopyroxene, while the outer layer adjacent to plagioclase primarily consists of clinopyroxene+spinel symplectite or less commonly amphibole+spinel symplectite. Locally, the clinopyroxene+spinel or amphibole+spinel symplectite layers are absent, with orthopyroxene and/or amphibole being the only coronae layers present.

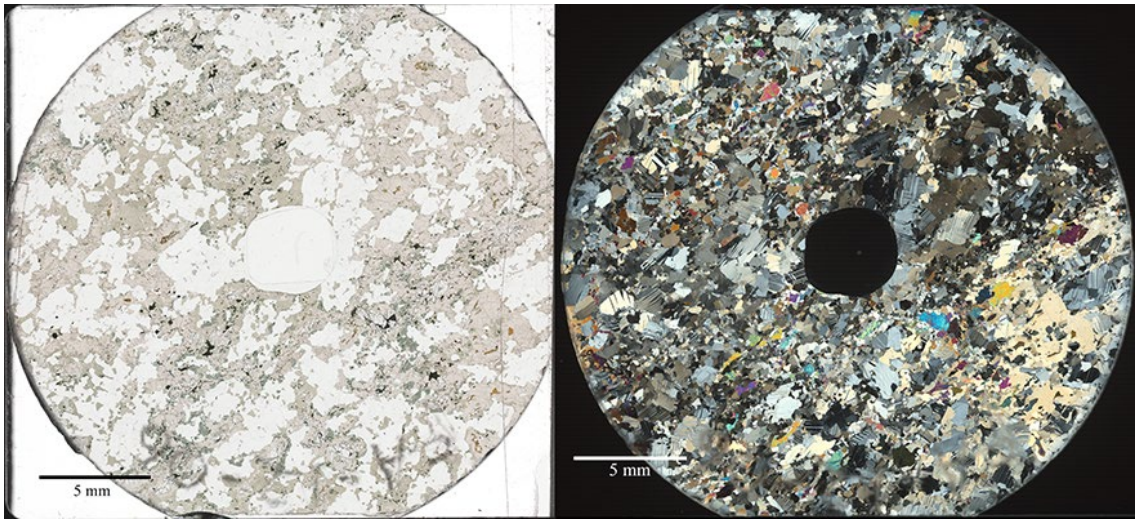

Figure 12 - FA1206: amphibole websterite, plane polarized thin section scan (left) and cross polarized (right).

Trace Element Mineral Chemistry

Rare earth elements (REEs) are a subset of the trace elements. REEs, being neighbors on the periodic table within the Lanthanide group, have very similar chemical and physical properties. This arises from an important characteristic the REEs share, a valence state of 3^+. Goldschmidt's rule on geochemical partitioning accounts for valence state (charge) and ionic radii; since charge is constant across the REEs this leaves the small but steady decrease in ionic size with increasing atomic number responsible for differences in chemical behavior. These small differences in size and behavior are affected by petrologic processes resulting in fractionation of the REE series relative to each other. This phenomenon is used in geochemistry to probe the petrogenetic history of samples and to assess the processes which came to form them. The REEs are among the least soluble trace elements, with their original concentrations being relatively stable through low-grade metamorphism and hydrothermal processes. The immobility of these elements under metamorphic conditions provides a useful means to assess the petrogenesis of the State Line granulite facies xenoliths**.** As shown by Michard (1989), hydrothermal fluids contain 5 x 10^2 and 10^6 less REE than the reservoir rock which they have passed through indicating that hydrothermal activity does not significantly affect original REE concentrations of rocks. The following trace element diagrams are shown with the typical order of elements, more incompatible on the left transitioning to more compatible on the right.

Clinopyroxene

Trace element data for SH-E1 clinopyroxene was reduced using EMP derived Calcium content as the normalization isotope and shows minor variability among the grains analyzed for rare earth elements **(Fig. 13).** The shape of the profile is arched with a positive slope for the light rare earth elements (LREE) and negative slope for the heavy rare earth elements (HREE). Variability of concentration across the entire REE profile is approximately two orders of magnitude. Variability of elemental concentration among the spots analyzed is no greater than half an order of magnitude with the largest variations for La, Sm, Er, Yb, Lu. The average La/Yb ratio is calculated as 0.23. A negligible depletion in Eu is present with an average Eu* value of 0.99. Eu*, or Eu anomaly, is a measurement of difference among the REE pattern and calculated with: $[Eu] / ([Sm]*[Gd])^{0.5}$.

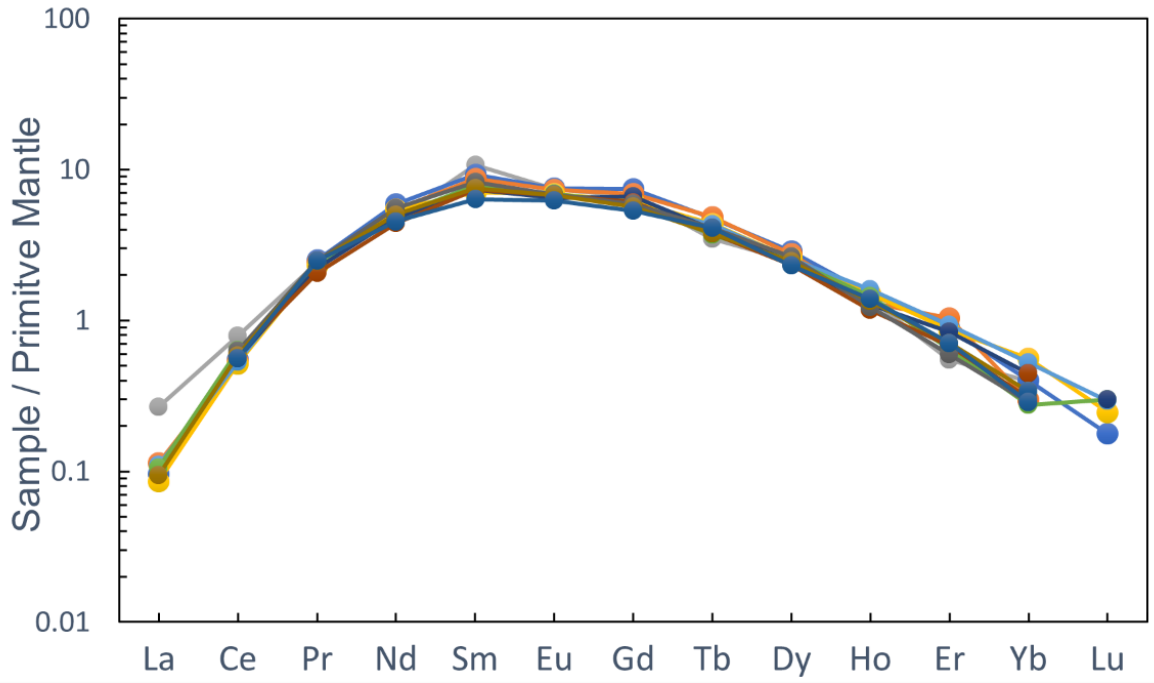

Figure 13 - REE diagram for SH-E1 clinopyroxene, individual analyses. Primitive mantle normalization values from McDonough and Sun (1995).

Trace element data for SD2-LC71 clinopyroxene was reduced using EMP derived Calcium content as the normalization isotope and varies by about half an order of magnitude with slightly more variation among the elements on the compatible side of the diagram **(Fig. 14).** The general shape of the profile is arched with a positive slope for the light rare earth elements and negative slope for the heavy rare earth elements. Variability of concentration across the entire REE profile is approximately two orders of magnitude. The lowest elemental concentrations occur within the HREE side of the profile with Lu at the lowest with an average concentration slightly above the average primitive mantle composition and an average La/Yb ratio of 5.19. Variability of elemental concentration among the spots analyzed is no greater than half an order of magnitude with the largest variations for La, Dy, Ho, Er, Yb, Lu. A minor depletion in Eu is present across all analyses with an average Eu* value of 0.63.

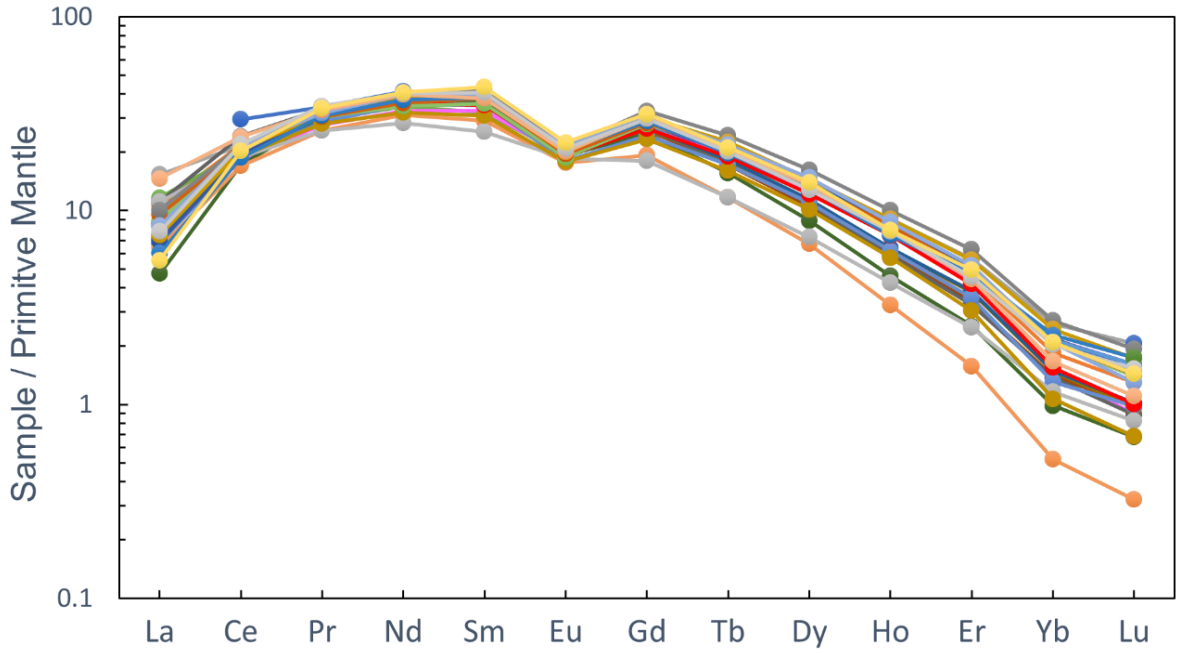

Figure 14 - REE diagram for SD2-LC71 clinopyroxene, individual analyses. Primitive mantle normalization values from McDonough and Sun (1995).

Trace element data for SD2-L110 clinopyroxene was reduced using EMP derived Calcium content as the normalization isotope and varies by about half an order of magnitude with more variation among the most and least compatible elements **(Fig. 15).** The general shape of the profile is arched with a positive slope for the LREE and negative slope for the HREE. Variability of concentration across the entire REE profile is approximately three orders of magnitude. The lowest elemental concentrations occur within the HREE side of the profile with Lu at the lowest with an average concentration half that of average primitive mantle composition and an average La/Yb ratio of 56.56. Variability of elemental concentration among the spots analyzed is no greater than half an order of magnitude with the largest variations for La, Ce, Ho, Er, Yb, Lu. A slight depletion in Eu is present across all analyses with an average Eu* value of 0.79.

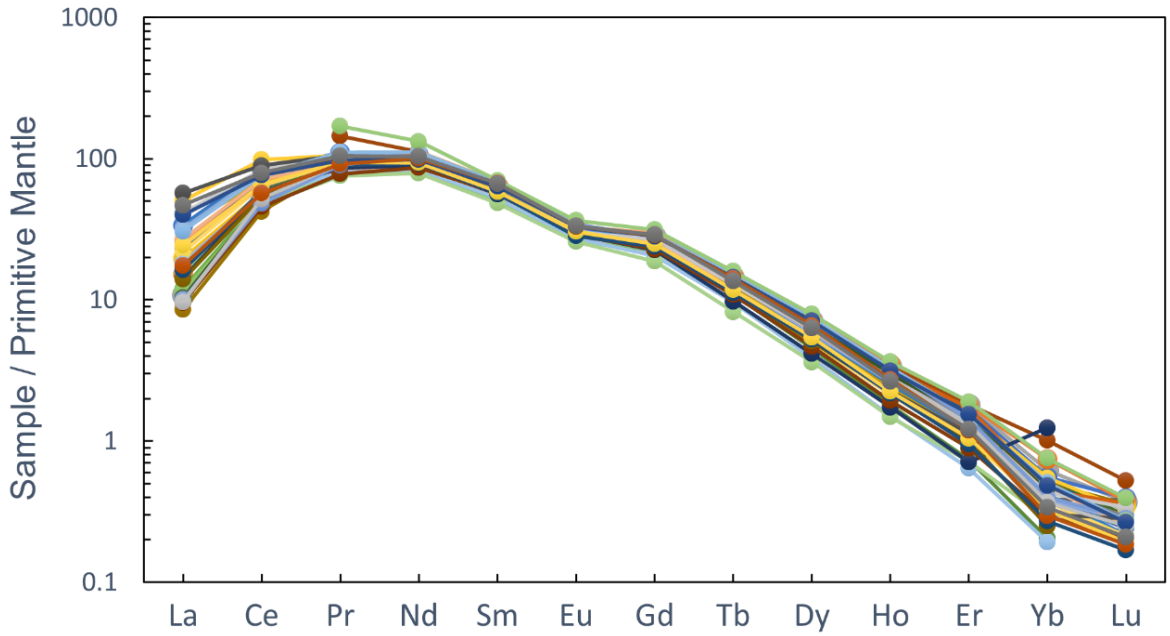

Figure 15 - REE diagram for SD2-L110 clinopyroxene, individual analyses. Primitive mantle normalization values from McDonough and Sun (1995).

Trace element data for SD2-LC120 clinopyroxene was reduced using EMP derived Calcium content as the normalization isotope and varies by about half an order of magnitude with more variation among the most compatible elements **(Fig. 16).** The general shape of the profile is arched with a positive slope for the LREE and negative slope for the HREE. The variability of concentrations across the entire REE profile is about one order of magnitude. The lowest elemental concentrations occur within the HREE side of the profile with Lu at the lowest with an average concentration approximately 5 times the average primitive mantle composition and an average La/Yb ratio of 1.96. Variability of elemental concentration among the spots analyzed increases with element compatibility with the largest variations for Dy, Ho, Er, Yb, Lu. Eu depletion is present across all analyses with an average Eu* value of 0.54.

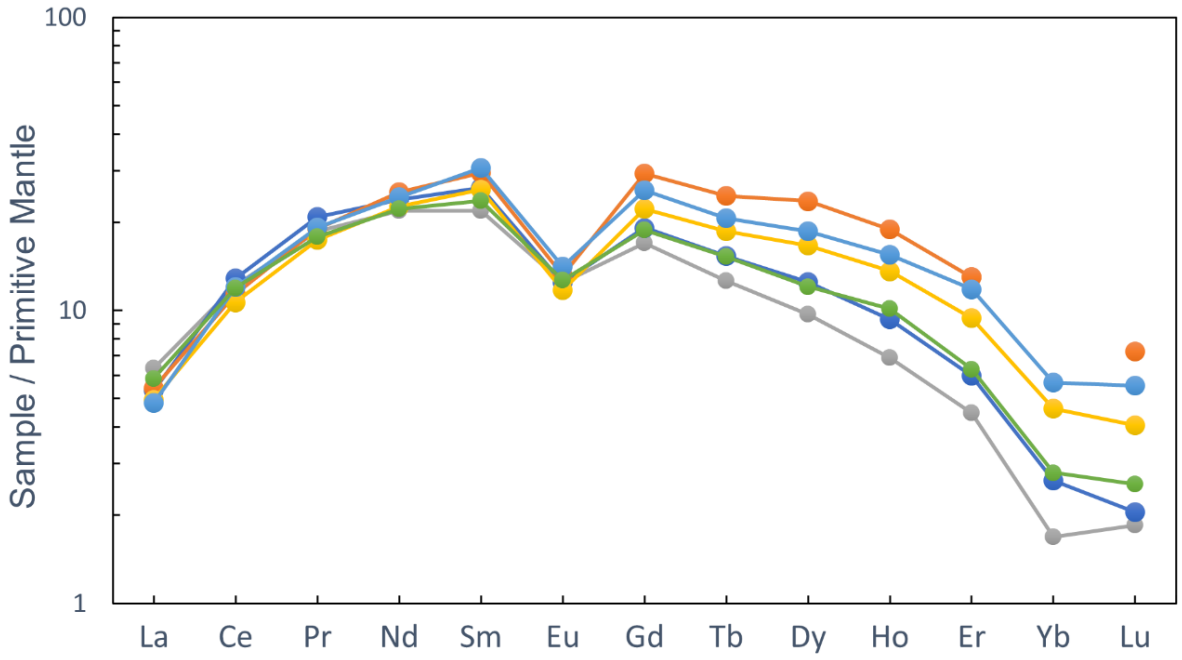

Figure 16 - REE diagram for SD2-LC120 clinopyroxene, individual analyses. Primitive mantle normalization values from McDonough and Sun (1995).

To directly compare the sample set, the average clinopyroxene data per sample is plotted together in **(Fig. 17)** and **(Fig. 18)**. All samples display a general arched profile with a positive slope among the LREE and negative slope for the HREE. SD2-LC120 expresses the largest Eu anomaly and a flatter profile than any other sample. SH-E1 is the most depleted of the sample set particularly within the LREE elements, owing to its high garnet content. SD2-L110 exhibits the highest LREE content yet is relatively depleted within the HREE, encompassing the largest La/Yb ratio by a significant margin.

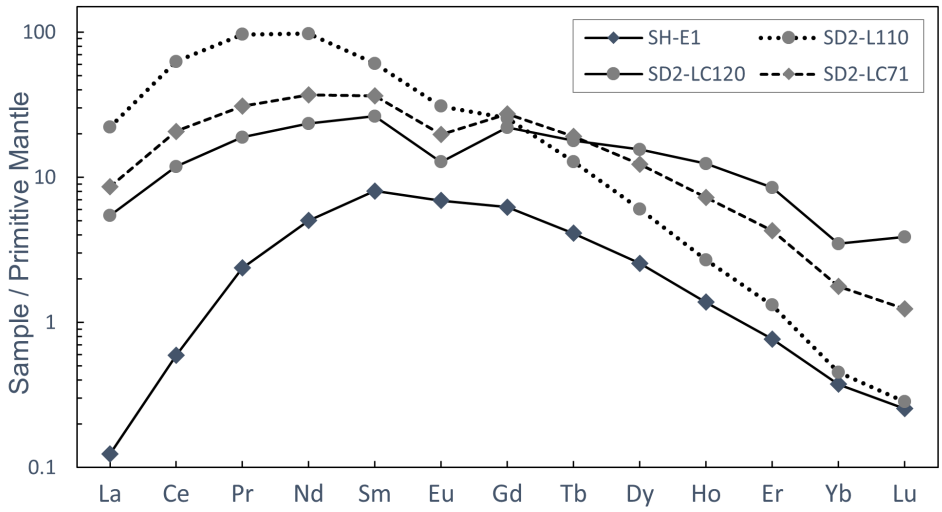

Figure 17 - REE diagram for all State Line clinopyroxene, average of all spots analyzed per sample. Primitive mantle normalization values from McDonough and Sun (1995).

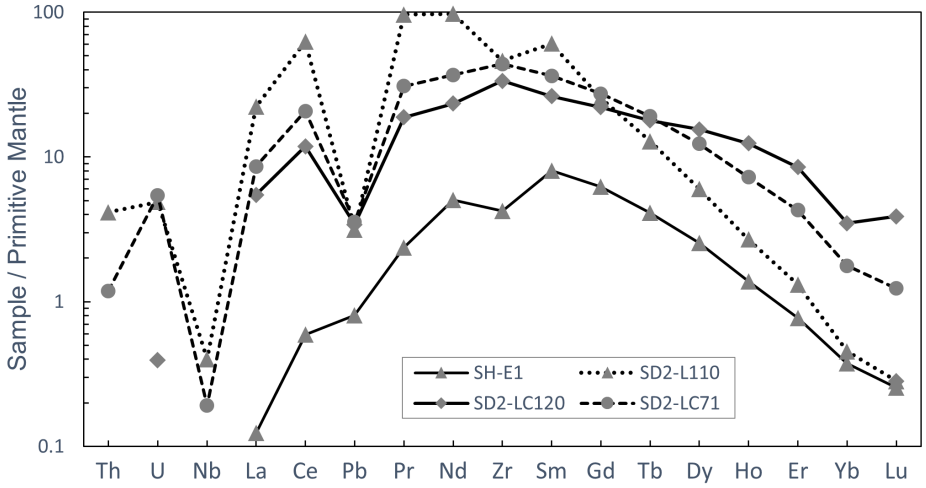

Figure 18- Incompatible trace element (ITE) diagram for all State Line clinopyroxene, average of all spots analyzed per sample. Primitive mantle normalization values from McDonough and Sun (1995).

Table 2 – Average clinopyroxene trace element data per sample, values reported in ppm.

	SH-E1	SD2-L110	SD2-LC71	SD2-LC120
n	11	45	28	6
Li	7.63	b.d.l.	b.d.l.	27.12
Sc	37.19	37.39	100.10	209.60
Ti	1217.54	4369.23	2943.73	4247.71
V	475.20	292.09	457.78	748.83
Cr	677.12	910.06	231.71	933.61
Co	31.25	b.d.l.	b.d.l.	45.92
Ni	205.86	97.41	66.46	110.30
Rb	3.85	159.52	268.08	b.d.l.
Sr	151.53	b.d.l.	b.d.l.	31.11
Y	4.99	10.30	25.55	36.13
Zr	44.37	484.61	460.63	352.44
Nb	b.d.l.	0.26	0.13	b.d.l.
Cs	0.66	b.d.l.	b.d.l.	b.d.l.
Ba	22.64	b.d.l.	b.d.l.	0.25
La	0.08	14.40	5.56	3.54
Ce	0.99	104.88	34.72	19.83
Pr	0.60	24.49	7.84	4.78
Nd	6.29	121.68	46.06	29.20
Sm	3.26	24.63	14.77	10.67
Eu	1.06	4.75	3.03	1.96
Gd	3.38	13.85	14.87	11.99
Tb	0.41	1.27	1.89	1.77
Dy	1.72	4.06	8.29	10.46
Ho	0.21	0.40	1.08	1.85
Er	0.34	0.58	1.88	3.72
Tm	0.03	0.05	0.17	0.41
Yb	0.16	0.20	0.78	1.54
Lu	0.02	0.02	0.08	0.26
Hf	2.19	b.d.l.	b.d.l.	25.18
Ta	b.d.l.	0.13	0.02	0.01
Pb	0.12	0.47	0.54	0.51
Th	b.d.l.	0.33	0.09	b.d.l.
U	b.d.l.	0.10	0.11	0.01

Garnet

Trace element data for SH-E1 garnet was reduced using EMP derived Calcium content as the normalization isotope and shows minor variability among the grains analyzed for rare earth elements **(Fig. 19)**. Concentrations for La, Ce, Pr were not resolvable as they were below the detection limit of the instrument. Variability of concentration across the entire REE profile is approximately two orders of magnitude. The La/Yb ratio cannot be quantified due to the lack of sufficient La data. A minor depletion in Eu is present with an average Eu* value of 0.88.

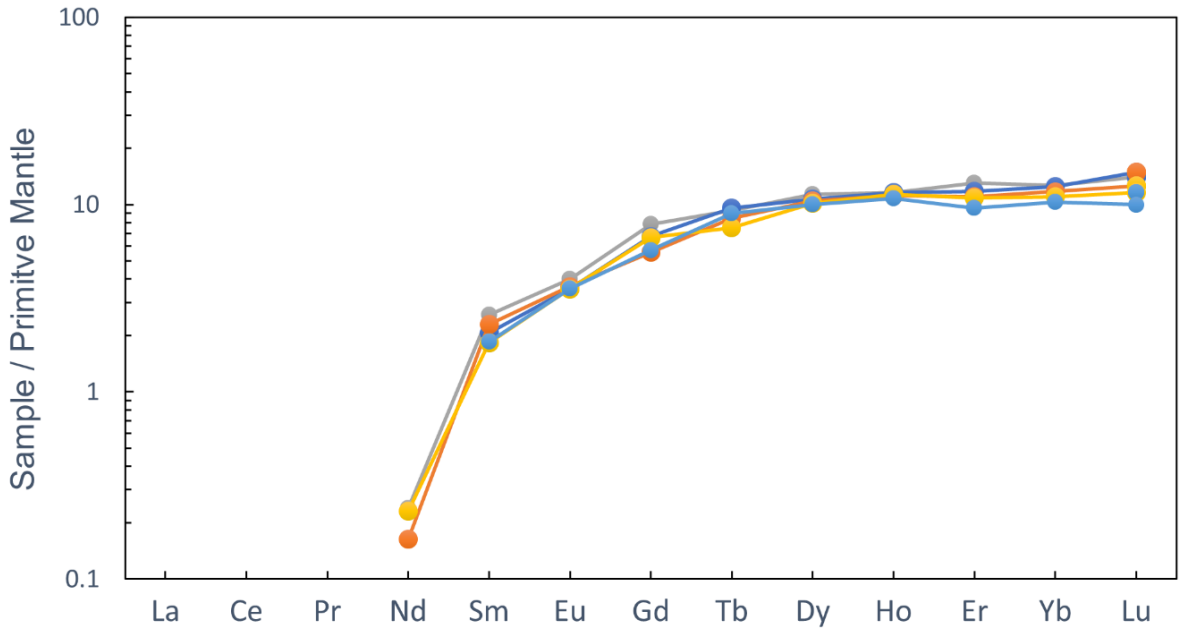

Figure 19 - REE diagram for SH-E1 garnet, individual analyses. Primitive mantle normalization values from McDonough and Sun (1995).

Trace element data for SD2-LC71 garnet was reduced using EMP derived Calcium content as the normalization isotope and varies by approximately one order of magnitude with significantly more variation among the elements on the incompatible side of the diagram **(Fig. 20)**. Variability of concentration across the entire REE profile is approximately four orders of magnitude. The lowest elemental concentrations occur within the LREE with La corresponding to the minimum. Average La/Yb ratio is calculated as 0.0046, indicating major depletion among the LREE with respect to HREE. Variability of elemental concentration among the spots analyzed is no greater than one and a half orders of magnitude with the largest variation for La by a significant margin. A minor depletion in Eu is present across all analyses with an average Eu* value of 0.63, equivalent to the Eu* value calculated for SD2-LC71 clinopyroxene.

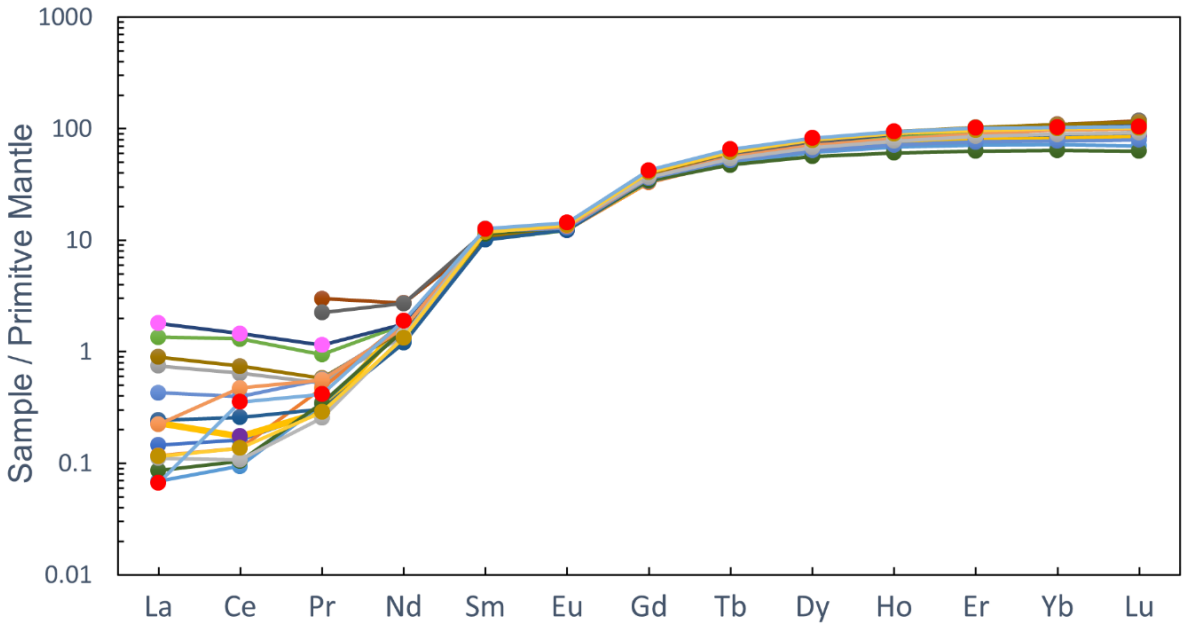

Figure 20 – REE diagram for SD2-LC71 garnet, individual analyses. Primitive mantle normalization values from McDonough and Sun (1995).

Trace element data for SD2-L110 garnet was reduced using EMP derived Calcium content as the normalization isotope and exhibits a positive slope which shallows and becomes slightly negative among the HREE **(Fig. 21**). Variability of concentration across the entire REE profile is approximately three orders of magnitude. The lowest elemental concentrations occur within the LREE with La, Ce, or Pr corresponding to the minimum. Average La/Yb ratio is calculated as 0.07, indicating significant depletion among the LREE with respect to HREE. The variability of elemental concentration among the spots analyzed is no greater than two orders of magnitude with the largest variations for La and Ce, by a significant margin. A minor depletion in Eu is present across all analyses with an average Eu* value of 0.76, roughly equivalent to the Eu* value calculated for SD2-L110 clinopyroxene.

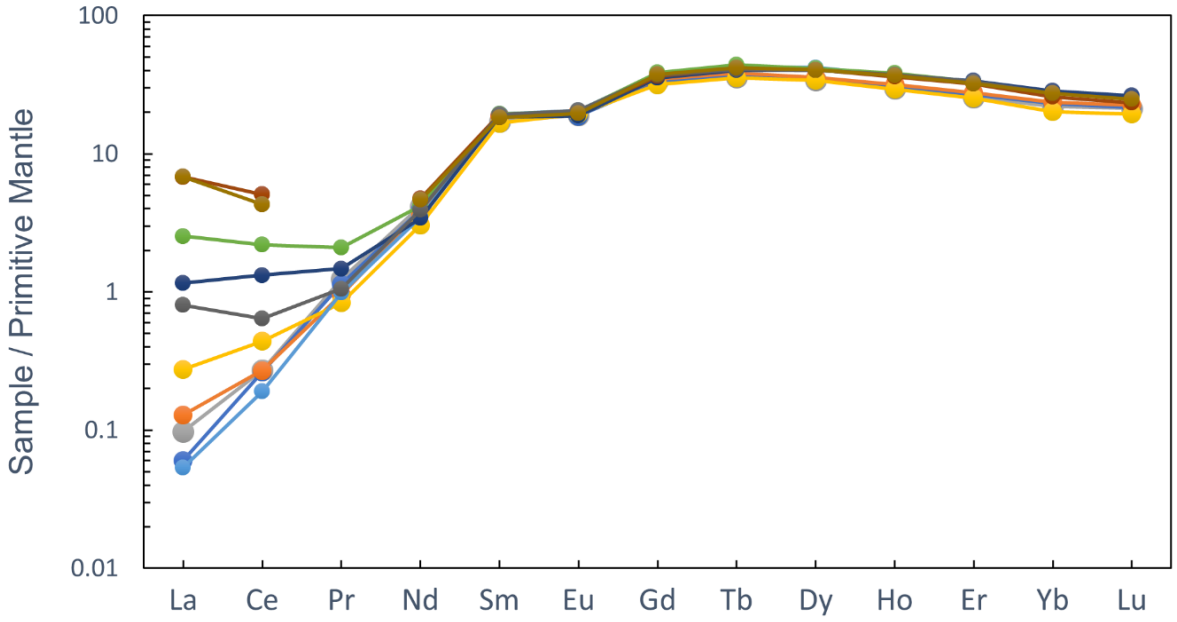

Figure 21 - REE diagram for SD2-L110 garnet, individual analyses. Primitive mantle normalization values from McDonough and Sun (1995).

Trace element data for SD2-LC120 garnet was reduced using EMP derived Calcium content as the normalization isotope and exhibits a positive slope which shallows and becomes negative among the HREE **(Fig. 22).** Variability of concentration across the entire REE profile is approximately one and a half orders of magnitude. The lowest elemental concentrations occur within the LREE with La, Ce, or Pr corresponding to the minimum. The average La/Yb ratio is calculated as 0.62 though significant variability in this ratio is recorded across the spots analyzed with a minimum of 0.17 and maximum of 1.34. The variability of elemental concentration among the spots analyzed is no greater than one order of magnitude with the largest variations for Ce and the HREE.

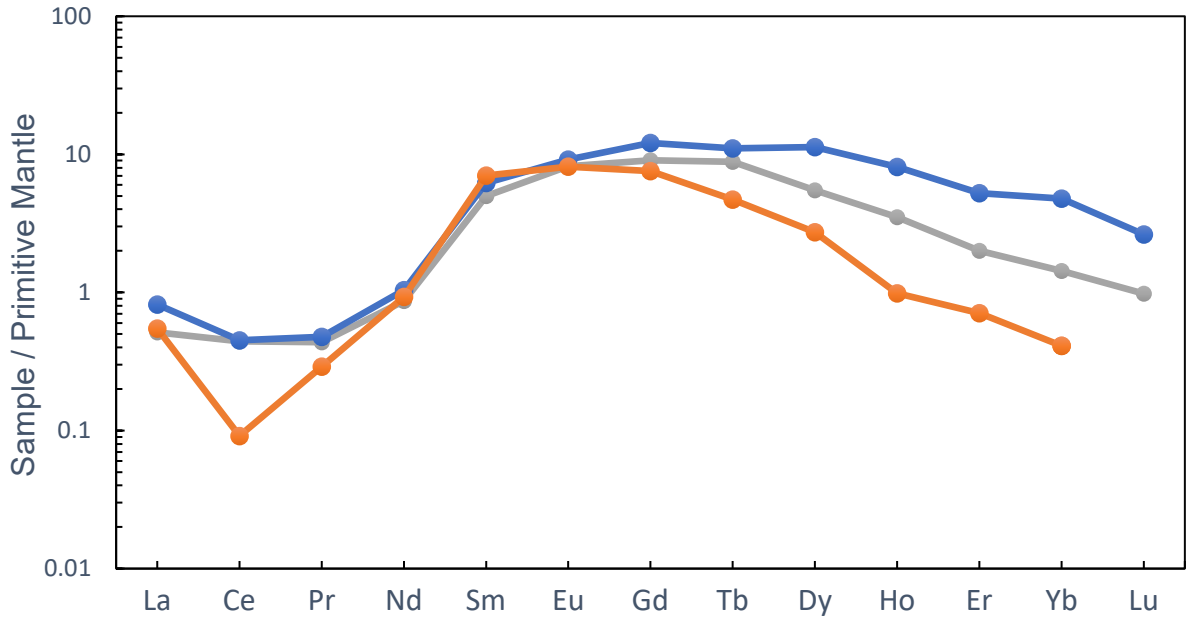

Figure 22 - REE diagram for SD2-LC120 garnet, individual analyses. Primitive mantle normalization values from McDonough and Sun (1995).

To directly compare the sample set, the average garnet data per sample is plotted together in **(Fig. 23)** and **(Fig. 24)**. All samples show enrichment of HREE with respect to LREE, a typical feature of garnet REE partitioning. SH-E1 and SD2-LC71 express progressive enrichment with element compatibility. SD2-LC120 and SD2-L110 maintain a positive slope through the LREE transitioning into a negative slope for the HREE. La/Yb ratios vary; SD2-LC71 has the highest ratio at 0.005 and SD2-LC120 the lowest at 0.62. All samples with definable La data show a slight enrichment in La with respect to Ce, resulting in a slope inflection among the LREE before enrichment towards more compatible trace elements.

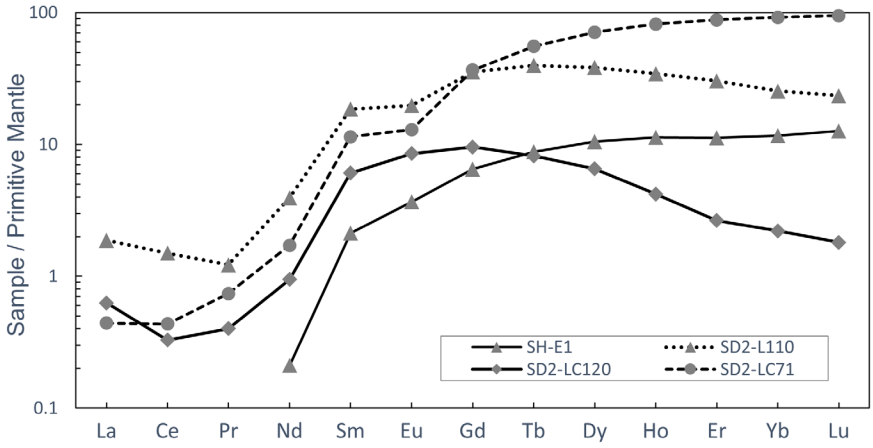

Figure 23 - REE diagram for all State Line garnet grains, average per sample. Primitive mantle normalization values from McDonough and Sun (1995).

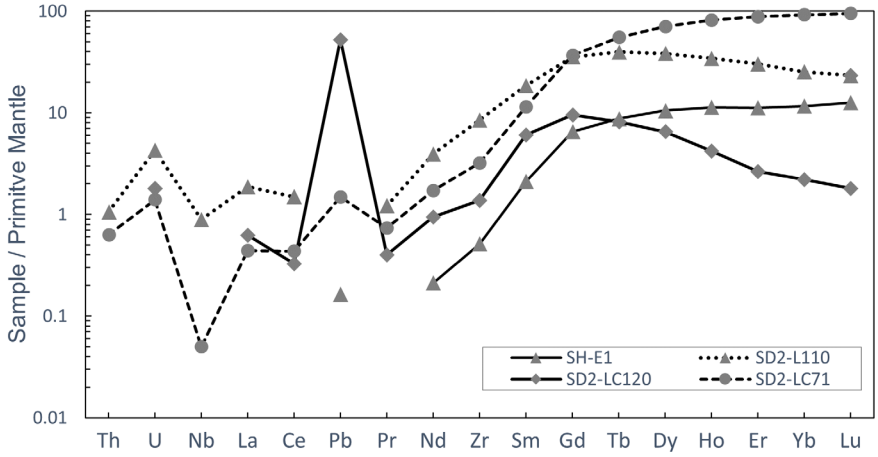

Figure 24 - ITE diagram for all State Line garnet grains, average per sample. Primitive mantle normalization values from McDonough and Sun (1995).

Table 3 - Average garnet trace element data per sample, values reported in ppm.

	SH-E1	SD2-L110	SD2-LC71	SD2-LC120
n	5	10	17	3
Sc	47.45	43.33	90.14	63.66
Ti	629.35	451.90	316.35	512.20
V	154.17	91.46	125.01	251.20
Cr	832.13	1175.35	190.16	60.32
Co	70.03	b.d.l.	b.d.l.	75.70
Ni	9.19	2.66	1.41	14.85
Rb	b.d.l.	83.35	151.44	30.88
Sr	0.06	b.d.l.	b.d.l.	262.56
Y	44.87	145.48	326.63	20.34
Zr	5.38	89.26	33.67	14.45
Nb	b.d.l.	0.59	0.03	b.d.l.
Cs	b.d.l.	b.d.l.	b.d.l.	0.74
Ba	b.d.l.	b.d.l.	b.d.l.	1869.99
La	b.d.l.	1.21	0.29	0.41
Ce	b.d.l.	2.51	0.73	0.55
Pr	b.d.l.	0.31	0.19	0.10
Nd	0.26	4.92	2.15	1.18
Sm	0.86	7.52	4.64	2.46
Eu	0.56	3.03	2.00	1.31
Gd	3.54	19.35	19.93	5.21
Tb	0.87	3.93	5.48	0.81
Dy	7.10	25.83	47.77	4.39
Ho	1.68	5.12	12.16	0.63
Er	4.93	13.29	38.59	1.16
Tm	0.71	1.67	5.70	0.13
Yb	5.13	11.17	40.60	0.97
Lu	0.85	1.58	6.41	0.12
Hf	0.10	b.d.l.	b.d.l.	0.27
Ta	b.d.l.	0.07	b.d.l.	b.d.l.
Pb	0.02	b.d.l.	0.22	7.89
Th	b.d.l.	0.08	0.05	b.d.l.
U	b.d.l.	0.09	0.03	0.04

Orthopyroxene

Orthopyroxene trace element data is less resolvable; having few individual spot analyses produce above detection limit values across the range of elements analyzed. Orthopyroxene ICPMS data was reduced using EMP derived Magnesium content as the normalization isotope.

SD2-L110 orthopyroxene data for the REE's is plotted in **(Fig. 25)**. Resolvable data points are sparse with only 3 individual spot analyses and much below detection limit. The general trend of the profile exhibits a negative slope among the REE's with primitive mantle comparable values for the LREE and approximately 1 order of magnitude below PM concentrations for HREE.

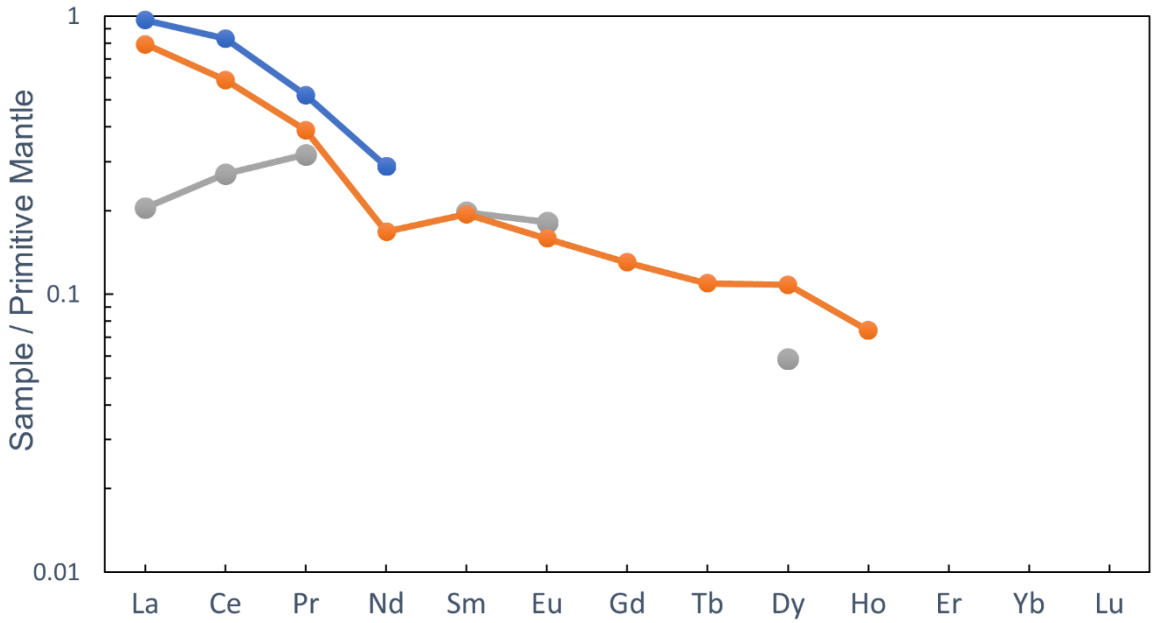

Figure 25 – REE Diagram: SD2-L110 orthopyroxene individual analyses. Primitive Mantle normalization values from McDonough and Sun (1995).

Trace element data for SD2-LC71 orthopyroxene exhibits a relatively flat profile with a shallow positive slope **(Fig. 26)**. The lowest elemental concentrations occur within the LREE with La, Ce, or Pr corresponding to the minimum. The average La/Yb ratio is calculated as 0.52 though significant variability in this ratio is recorded across the spots analyzed with a minimum of 0.295 and maximum of 1.01. 6 grains were analyzed in this sample across 13 spots. The variability of elemental concentration among the spots analyzed is no greater than one order of magnitude with the largest variations for La and the LREE.

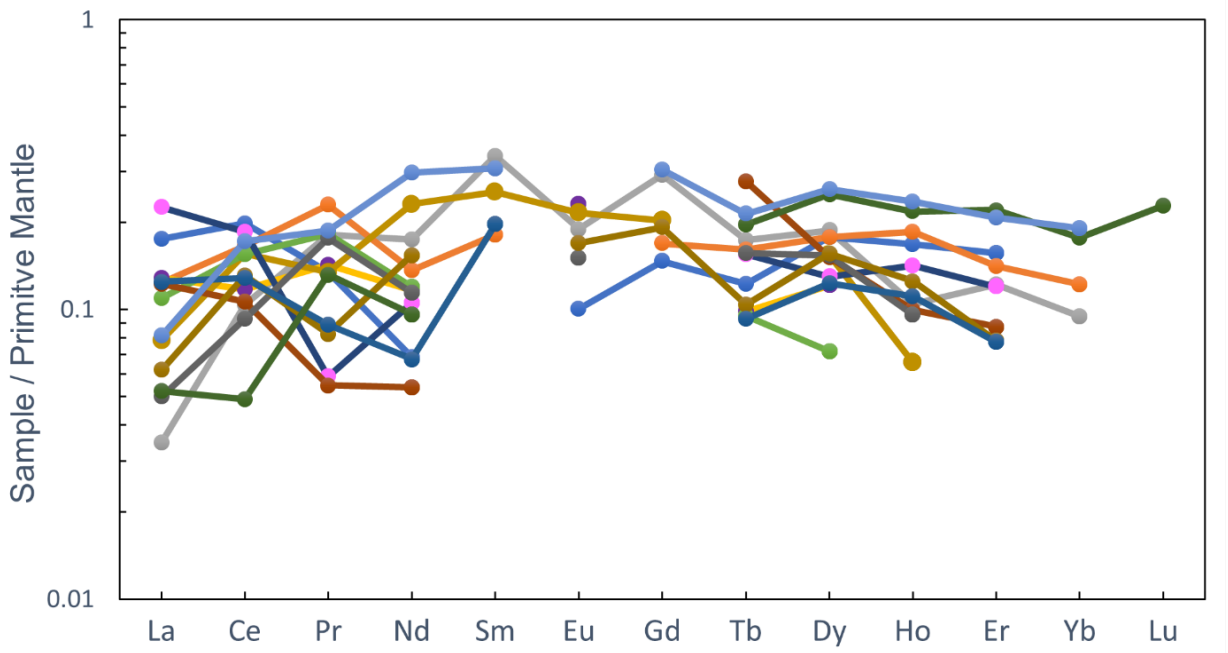

Figure 26 - REE diagram for SD2-LC71 orthopyroxene individual analyses. Primitive mantle normalization values from McDonough and Sun (1995).

To directly compare the sample set, the average orthopyroxene data per sample is plotted together in **(Fig. 27)** and **(Fig. 28)**. SD2-LC71 and SD2-LC120 show minor enrichment of HREE with respect to LREE, a typical feature of orthopyroxene REE partitioning. However, SD2-L110 exhibits a negative slope and though the data set is incomplete the trend is of decreased concentration with respect to element compatibility.

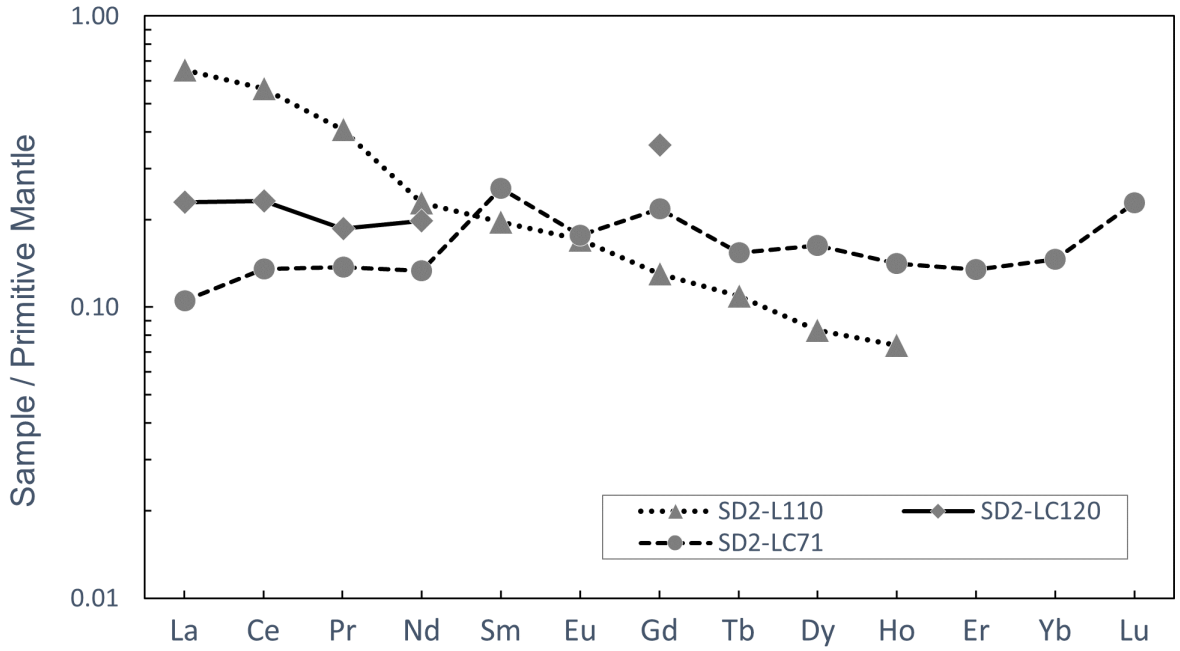

Figure 27 - REE diagram for all State Line orthopyroxene, grains average per sample. Primitive mantle normalization values from McDonough and Sun (1995).

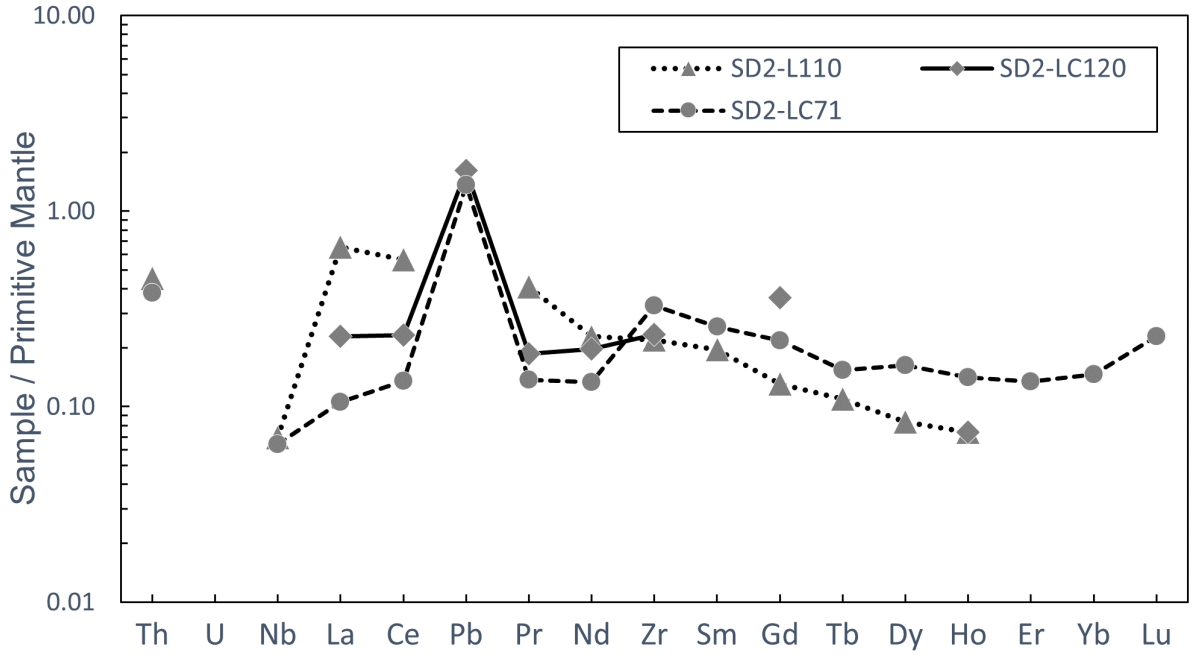

Figure 28 – ITE diagram for all State Line orthopyroxene grains, average per sample. Primitive mantle normalization values from McDonough and Sun (1995).

Table 4 - Average orthopyroxene trace element data per sample, values reported in ppm.

	SD2-L110	SD2-LC71	SD2-LC120
n	3	13	4
Li	b.d.l.	b.d.l.	9.04
Sc	3.95	9.33	10.50
Ti	402.76	391.84	369.87
V	61.60	90.43	511.69
Cr	267.59	69.91	479.95
Co	b.d.l.	b.d.l.	126.10
Ni	199.02	121.97	170.99
Rb	754.31	1254.67	18.24
Sr	b.d.l.	b.d.l.	2.11
Y	0.15	0.56	0.14
Zr	2.30	3.44	2.45
Nb	0.05	0.04	b.d.l.
Cs	b.d.l.	b.d.l.	0.28
Ba	b.d.l.	b.d.l.	12.11
La	0.42	0.07	0.15
Ce	0.94	0.23	0.39
Pr	0.10	0.03	0.05
Nd	0.28	0.17	0.25
Sm	0.08	0.10	b.d.l.
Eu	0.03	0.03	b.d.l.
Gd	0.07	0.12	0.20
Tb	0.01	0.02	b.d.l.
Dy	0.06	0.11	b.d.l.
Ho	0.01	0.02	b.d.l.
Er	b.d.l.	0.06	b.d.l.
Tm	b.d.l.	0.01	b.d.l.
Yb	b.d.l.	0.06	b.d.l.
Lu	b.d.l.	0.02	b.d.l.
Hf	b.d.l.	b.d.l.	0.18
Ta	b.d.l.	0.02	b.d.l.
Pb	b.d.l.	0.20	0.24
Th	0.04	0.03	b.d.l.
U	b.d.l.	b.d.l.	b.d.l.

Plagioclase

Plagioclase trace element data is limited; having few individual spot analyses produce above detection limit values across the range of elements analyzed. Plagioclase ICPMS data was reduced using EMP derived Calcium content as the normalization isotope.

Trace element data for SD2-L110 plagioclase is plotted in **(Fig. 29)**. Resolvable data points are sparse with 4 individual spot analyses and much below detection limit. The general trend of the profile exhibits a negative slope among the REE's with significant enrichment of the LREE's with respect to primitive mantle values and an average Eu* of 9.36.

SD2-LC71 plagioclase data for the REE's is plotted in **(Fig. 30)**. Resolvable data points are sparse with only 2 individual spot analyses and much below detection limit.

To directly compare the sample set, the average plagioclase data per sample is plotted together in **(Fig. 31)** and **(Fig. 32)**. All samples show minor enrichment of Eu and LREE with respect to HREE, a typical feature of plagioclase REE partitioning.

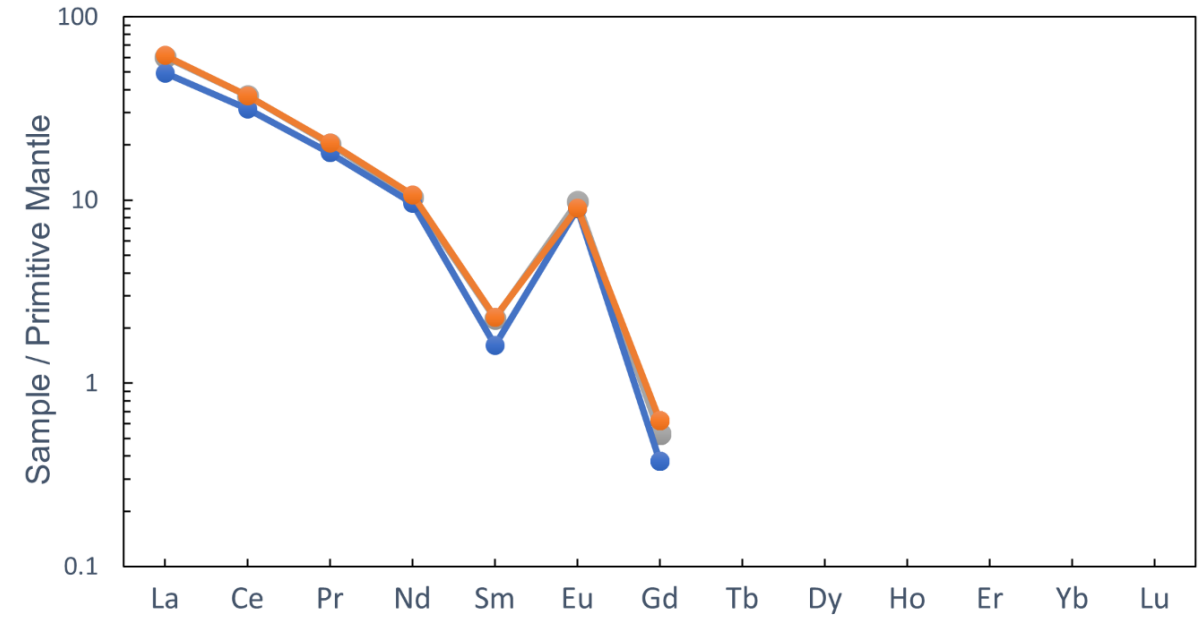

Figure 29 – REE diagram for SD2-L110 plagioclase individual spot analyses. Primitive mantle normalization values from McDonough and Sun (1995).

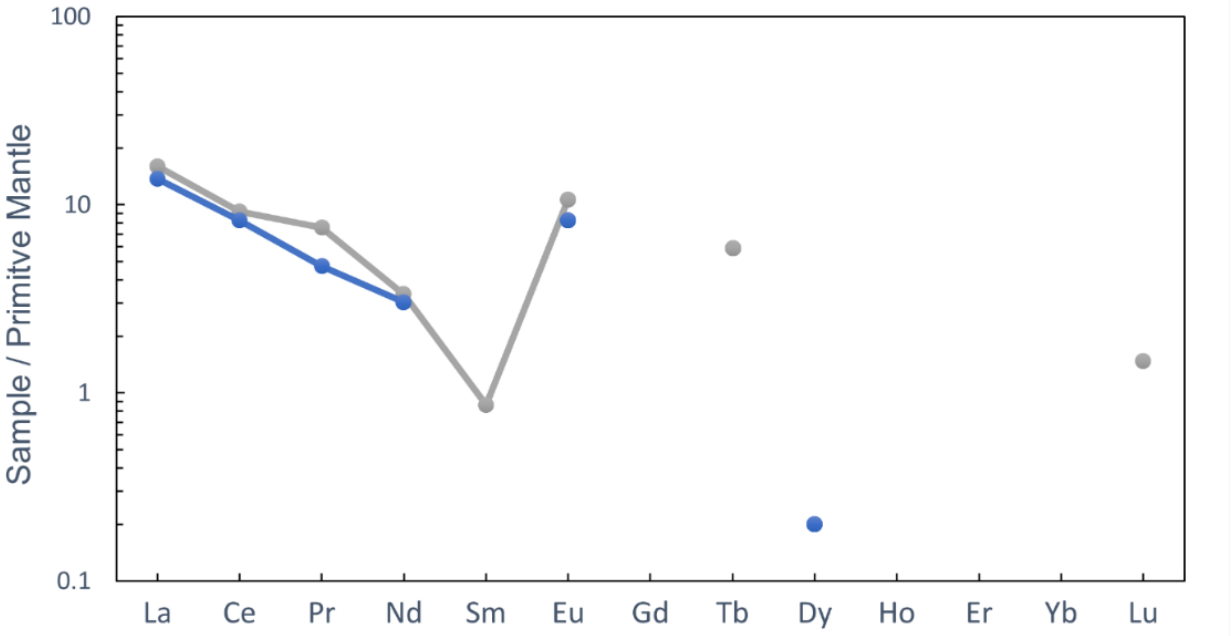

Figure 30 - REE diagram for SD2-LC71 plagioclase individual spot analyses. Primitive mantle normalization from McDonough and Sun (1995).

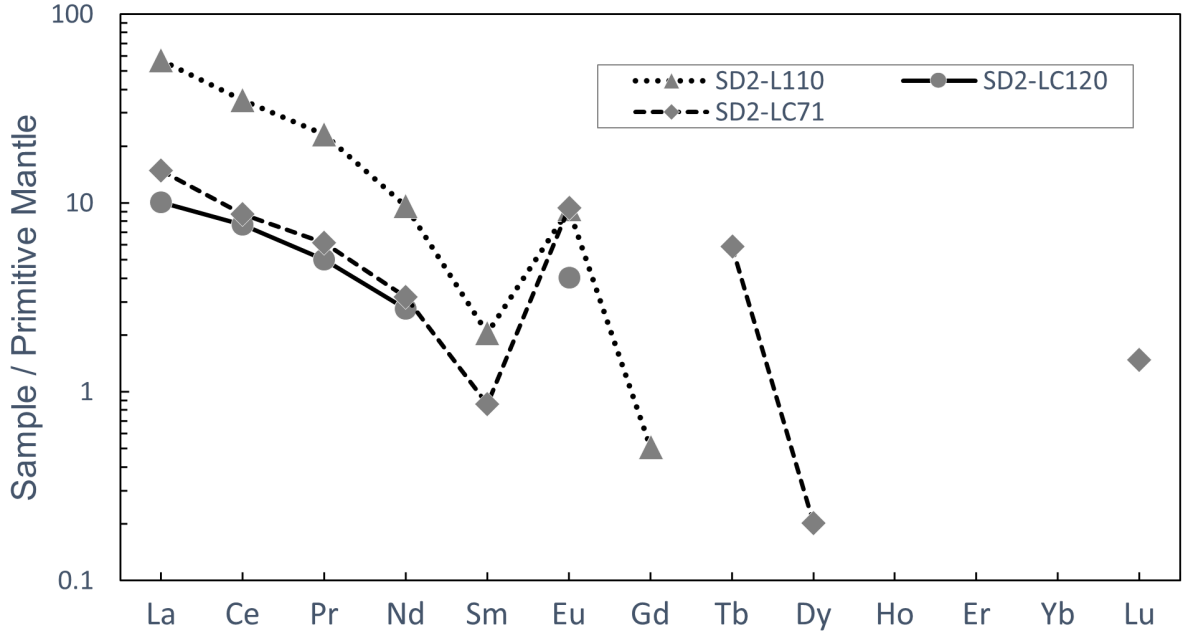

Figure 31 - REE diagram for all State Line plagioclase grains, average per sample. Primitive mantle normalization values from McDonough and Sun (1995).

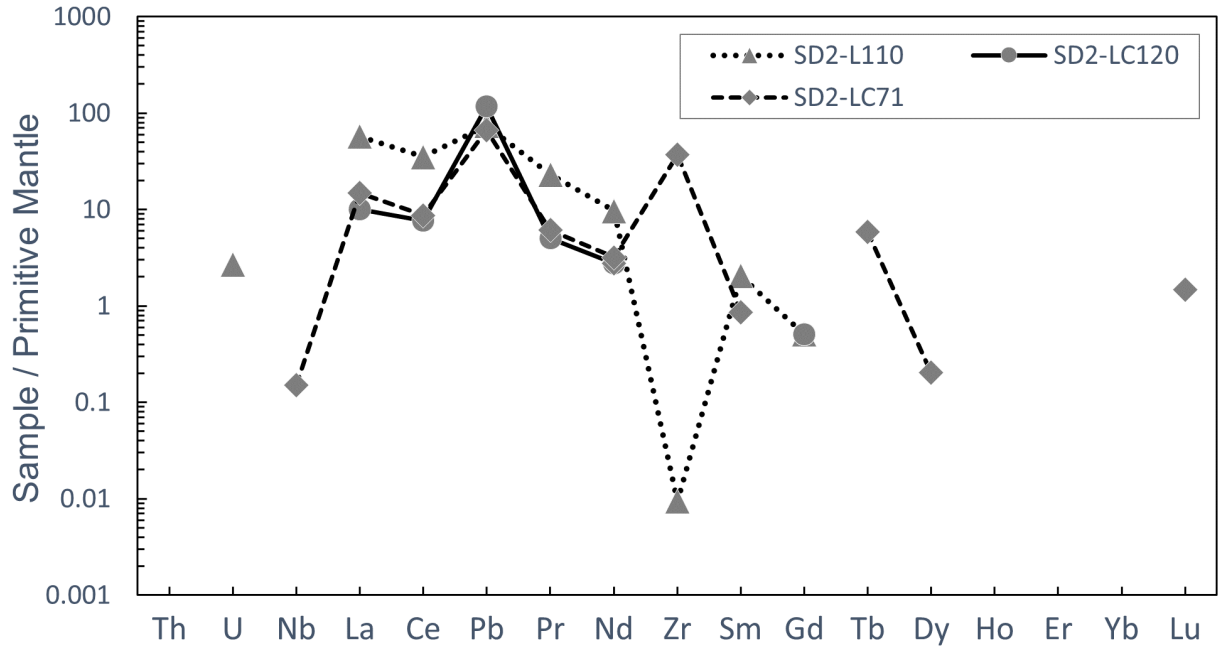

Figure 32 - ITE diagram for all State Line plagioclase grains, average per sample. Primitive mantle normalization from McDonough and Sun (1995).

Table 5 - Average plagioclase trace element data per sample, values reported in ppm.

	SD2-L110	SD2-LC71	SD2-LC120
n	4	2	1
Li	b.d.l.	b.d.l.	5.98
Sc	b.d.l.	b.d.l.	9.14
Ti	98.84	65.13	342.62
V	b.d.l.	b.d.l.	b.d.l.
Cr	b.d.l.	b.d.l.	b.d.l.
Co	b.d.l.	b.d.l.	1.68
Ni	2.94	1.64	1.26
Rb	b.d.l.	b.d.l.	b.d.l.
Sr	b.d.l.	b.d.l.	1170.57
Y	0.11	0.91	b.d.l.
Zr	0.10	388.90	b.d.l.
Nb	b.d.l.	0.10	b.d.l.
Cs	b.d.l.	b.d.l.	b.d.l.
Ba	b.d.l.	b.d.l.	65.72
La	36.96	9.61	6.52
Ce	58.80	14.57	12.88
Pr	5.86	1.56	1.27
Nd	12.07	3.98	3.44
Sm	0.83	0.35	b.d.l.
Eu	1.43	1.45	0.62
Gd	0.28	b.d.l.	b.d.l.
Tb	b.d.l.	0.58	b.d.l.
Dy	b.d.l.	0.14	b.d.l.
Ho	b.d.l.	b.d.l.	b.d.l.
Er	b.d.l.	b.d.l.	b.d.l.
Tm	b.d.l.	b.d.l.	b.d.l.
Yb	b.d.l.	b.d.l.	b.d.l.
Lu	b.d.l.	0.10	b.d.l.
Hf	b.d.l.	b.d.l.	b.d.l.
Ta	b.d.l.	0.74	b.d.l.
Pb	11.00	9.91	17.74
Th	b.d.l.	b.d.l.	b.d.l.
U	0.05	b.d.l.	b.d.l.

Whole Rock Reconstruction

All reconstructed whole rock trace element compositions were calculated using in-situ mineral ICPMS data in conjunction with mineral modes derived EDS map pixel counting. Minerals used for these reconstructions are garnet, clinopyroxene, orthopyroxene, and plagioclase. While this method does exclude accessory minerals and oxides (e.g. apatite, ilmenite, rutile) which may contain appreciable concentrations of various trace elements; it also excludes host lava contamination along grain boundaries, fractures, and other zones of secondary alteration **(Fig. 38)**.

To directly compare the sample set, each whole rock reconstructed trace element profile is plotted together in **(Fig. 33)** and **(Fig. 34)**. Each sample displays a different general profile shape among the REE's with the only parallel trends evident among the incompatible trace elements (ITE's) Th, Nb, and U. SD2-LC120 exhibits a generally negative sloped profile with a small inflection about Eu and a La/Yb ratio of 4.77. SH-E1 displays a positively sloped profile which shallows among the HREE's and the most disproportionate La/Yb ratio of the sample set at a value of 0.011. SD2-L110 has a minimally arched profile with the highest LREE concentrations amongst the sample set, a minor Eu* anomaly calculated at 0.74, and a La/Yb ratio of 1.11. SD2-LC71 exhibits a positively sloped profile with the highest HREE concentrations among the sample set, a La/Yb ratio of 0.376 and minor Eu* anomaly of 0.78.

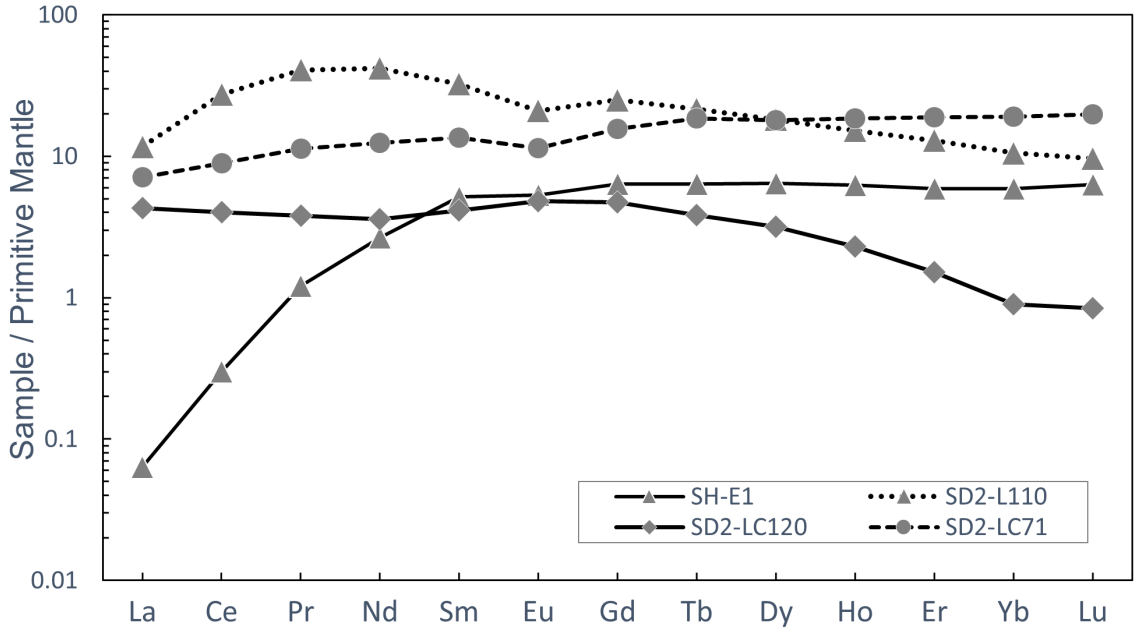

Figure 33 - Whole rock reconstructed REE values for State Line sample set. Mineral modes reported in Table 3. SH-E1: arclogite. SD2-LC120, SD2-LC71, SD2-L110: two-pyroxene granulite.

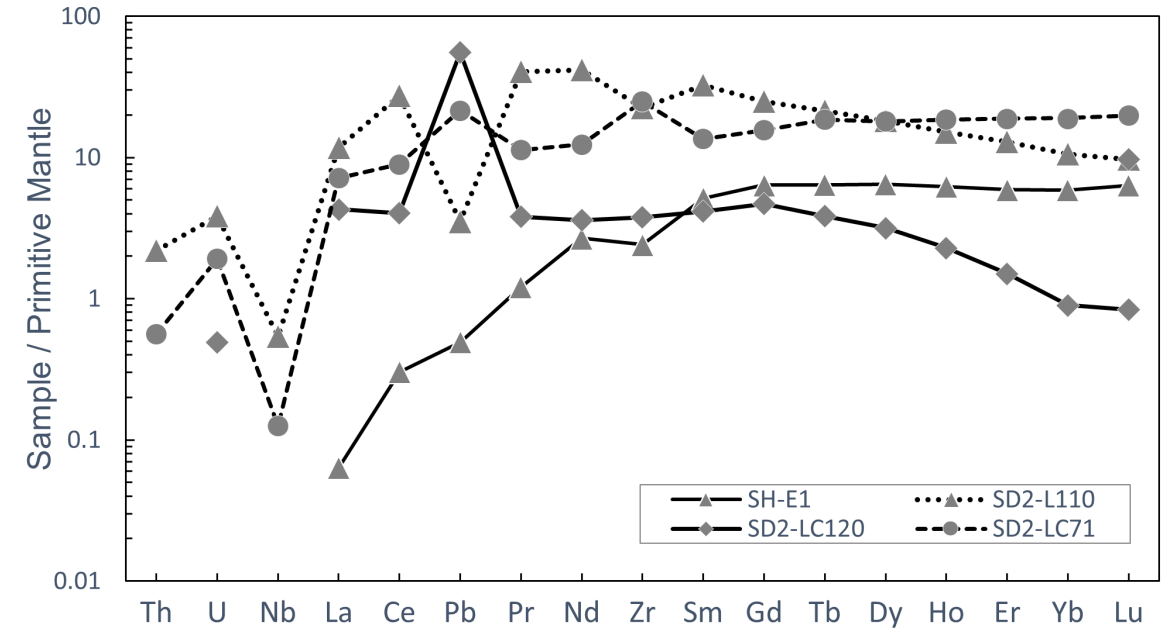

Figure 34 – Whole rock reconstructed ITE values for State Line sample set. Mineral modes reported in Table 3. SH-E1: arclogite. SD2-LC120, SD2-LC71, SD2-L110: two-pyroxene granulite.

Table 6 - Whole Rock reconstructed unnormalized trace element values for State Line samples, values reported in ppm

	SH-E1	SD2-L110	SD2-LC120	SD2-LC71
Th	0.00	0.17	0.00	0.04
U	0.00	0.08	0.01	0.04
Nb	0.00	0.35	0.00	0.09
Ta	0.00	0.08	0.00	0.32
La	0.04	7.57	2.78	5.65
Ce	0.50	45.78	6.75	15.99
Pb	0.07	0.53	8.31	4.37
Pr	0.31	10.32	0.96	2.89
Nd	3.34	52.09	4.50	14.95
Zr	25.27	234.58	39.59	298.42
Sm	2.09	13.16	1.68	5.08
Eu	0.82	3.23	0.74	1.80
Ti	929.45	2032.48	783.70	948.48
Gd	3.46	13.57	2.56	7.56
Tb	0.63	2.12	0.38	1.71
Dy	4.35	12.21	2.14	10.51
Ho	0.93	2.25	0.34	2.37
Er	2.58	5.66	0.66	7.09
Yb	2.60	4.64	0.40	7.13
Lu	0.43	0.65	0.06	1.16

Table 7 - State Line sample mineral modes determined through pixel counting.

	Garnet	Cpx	Opx	Plag
SH-E1	0.49	0.51	0.0	0.0
SD2-L110	0.41	0.41	0.15	0.03
SD2-LC120	0.25	0.10	0.30	0.35
SD2-LC71	0.17	0.28	0.11	0.42

SIMS Data – State Line

SIMS data is plotted with each point corresponding to a single grain **(Fig. 35)**. Points without error bars indicate a single analysis for a grain. Points with error bars indicate one standard deviation from the multiple analyses recorded within a single grain.

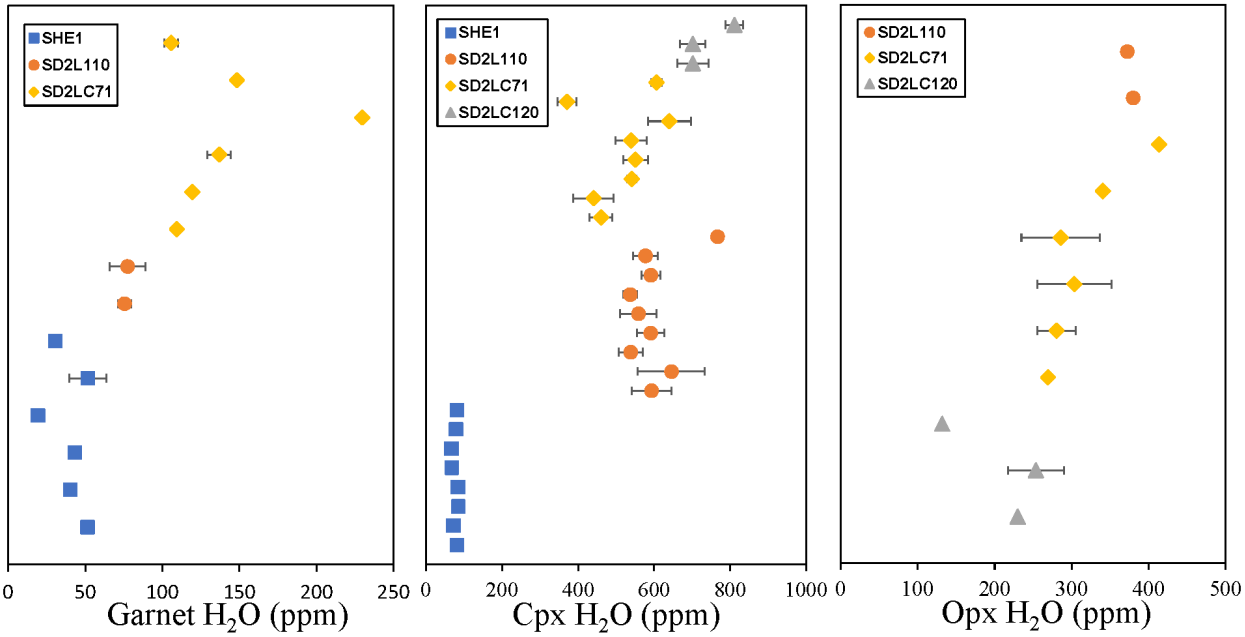

Figure 35 - State Line SIMS H_2O results reported in parts per million (ppm). Each data point represents a grain, error bars indicate one standard deviation from multiple analyses recorded within a single grain.

SIMS Data – Famatinia

SIMS data is plotted with each point corresponding to a single grain **(Fig. 36)**. Points without error bars indicate a single analysis for a grain. Points with black borders indicate one standard deviation from the multiple analyses recorded within a single grain with number of analyses, n, indicated along the y axis.

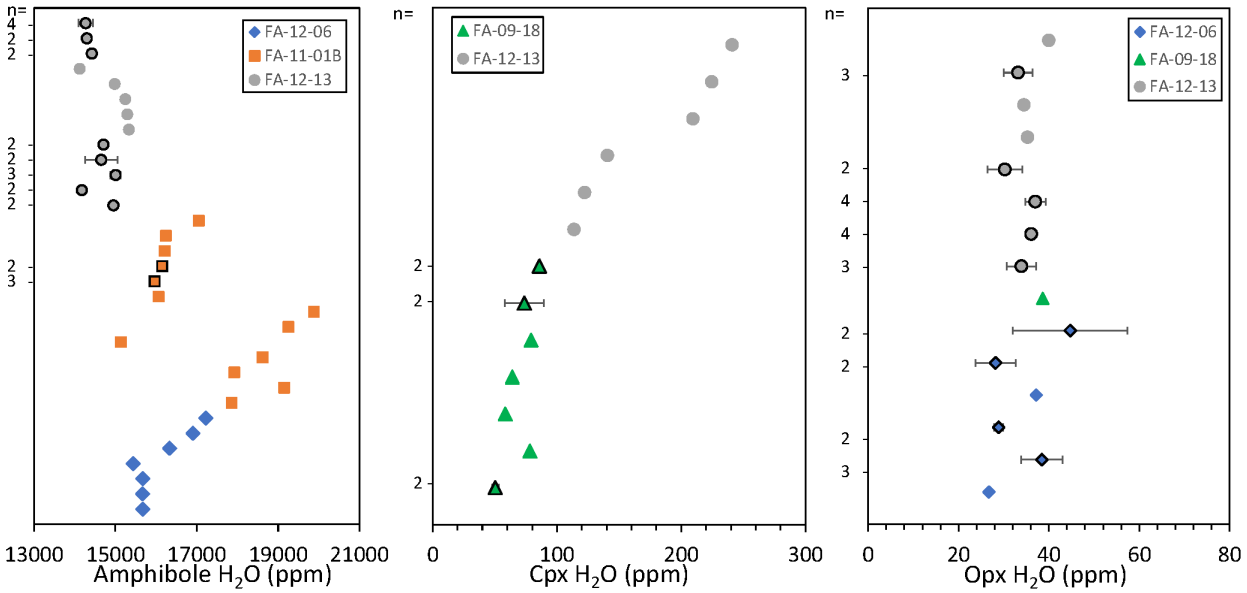

Figure 36 - Famatinia SIMS H_2O results reported in parts per million (ppm). Each data point represents a grain, error bars indicate one standard deviation from multiple analyses recorded within a single grain.

Discussion & Analysis

We find that while our two sample suites are both arc derived, the hydration state of NAMSs are up to an order of magnitude apart. While The Sierras de Valle Fértil is one of few continuous deep arc crust exposures worldwide with minimal deformation we propose that its hydration state may no longer reflects equilibrium condition within the lower crust due to its exhumation history. Regional scale exhumation of the terrane and accompanying retrograde metamorphism may have altered the original mineralogy, textures, and chemistry of the rocks. Alternatively, the age of formation and eruption for State Line xenoliths make them ideal for constraining water content of stable, undeformed, equilibrated lower continental crust; with regional deep lithosphere containing Paleoproterozoic age rocks and eruption of these xenoliths in the Devonian predating any potential metasomatism/overprinting during the Laramide orogeny.

In this section we will address hydration state and trace element chemistry of the State Line xenoliths, hydration state of the Famatinia samples, the petrogenetic similarities between

these two regions, and the unique complications that arise from analyzing these sample suites individually and as a comparative set. The goal of this discussion is to find commonalities between these settings and ways to better understand other subduction related lower crustal terranes around the globe.

Relationships between reconstructed water and trace element compositions

For the State Line xenoliths, whole rock trace element reconstructions exhibit considerable variability **(Fig. 33, 34)**. This variability can be primarily attributed to the mineralogic proportions which differ across the set of samples. Regardless, we do find indications that these samples originate from a shared magma source and thus likely represent a fractionation sequence (Chin et al., 2020).

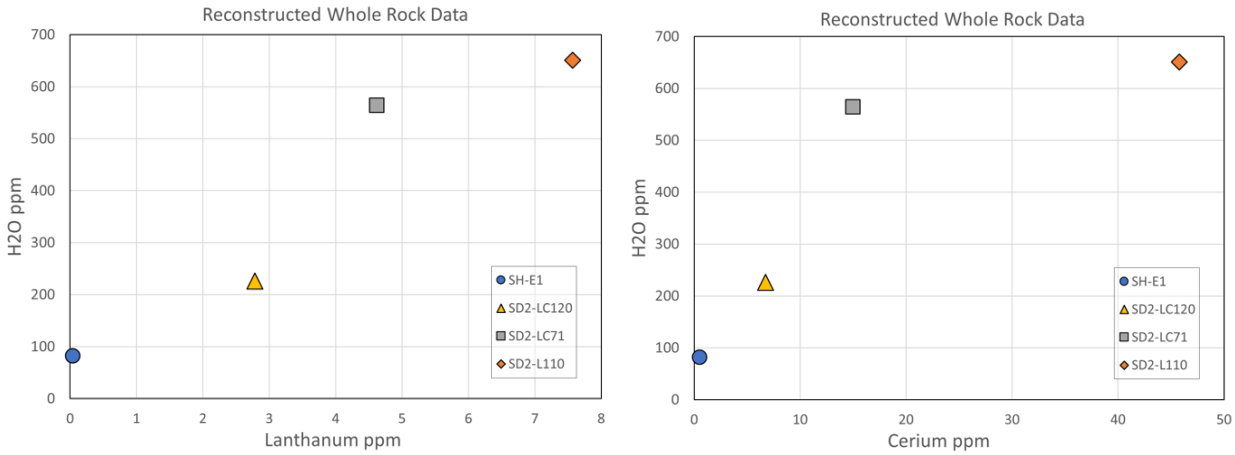

Figure 37 – Whole Rock reconstructed H_2O and REE concetrations for State Line samples.

When reconstructed whole-rock H_2O is plotted against reconstructed whole rock La and Ce, we observe strong positive trends **(Fig. 37)**. Both La and Ce are highly incompatible like H_2O (or OH, H^+) and Ce and H_2O have nearly identical partition coefficients (Michael, 1995). Thus, the fact that the State Line xenoliths are correlated in La, Ce vs. H_2O strongly suggests a common fractional crystallization history. Importantly, because the mineral diffusivities of La,

Ce, and REE are orders of magnitude slower than H^+ (Ingrin and Blanchard, 2006), any open-system process (e.g., late-stage degassing of the xenoliths during eruption) should generally re-equilibrate NAM H_2O contents to a uniform, low level, but this is not observed when examining the mineral data in detail because the ratio of H_2O in clinopyroxene/orthopyroxene is similar to high-T, experimental values (Chin et al. 2020).

Whole rock powder vs. EDS-based pixel counting reconstructions

Whole rock reconstructions were quantified using in-situ measurements of primary silicate minerals: garnet, clinopyroxene, orthopyroxene, and plagioclase. This data coupled with mineral modes determined from EDS based pixel counting provide a close approximation of whole rock chemistry though accessory mineral data could not be obtained and thus is not factored into these reconstructions.

Previous work on State Line xenoliths (Farmer et al., 2005) quantified the trace element composition of State Line samples using a methodology that involves powdering the sample and then doing bulk analyses on the rock powders. While this method does manage to capture the elemental contribution of all minerals in the sample including accessory minerals, it also captures any contribution from alteration/infiltration of host fluids and lava which incurred on exhumation/eruption of the xenoliths. Whole rock reconstructions using in-situ mineral data

coupled with modes derived from EDS-based pixel counting data avoid incorporating the chemical contribution of these altered portions of the samples.

When comparing the data quantified from the in-situ laser ablation methodology used in this study against previous studies using powder there is a significant discrepancy in the reported LREE **(Fig. 39)**. The LREE are the most affected owing to their high incompatibility compared to MREE and HREE **(Fig. 39)**. We propose that this discrepancy can be attributed to infiltration of fluids along the grain boundaries. EDS maps **(Fig. 38)** of the samples show that the grain boundaries of the State Line samples have been enriched in incompatible elements such as K. This potassium and incompatible element enrichment is likely associated with grain boundary alteration due to interaction with kimberlitic host during exhumation/eruption.

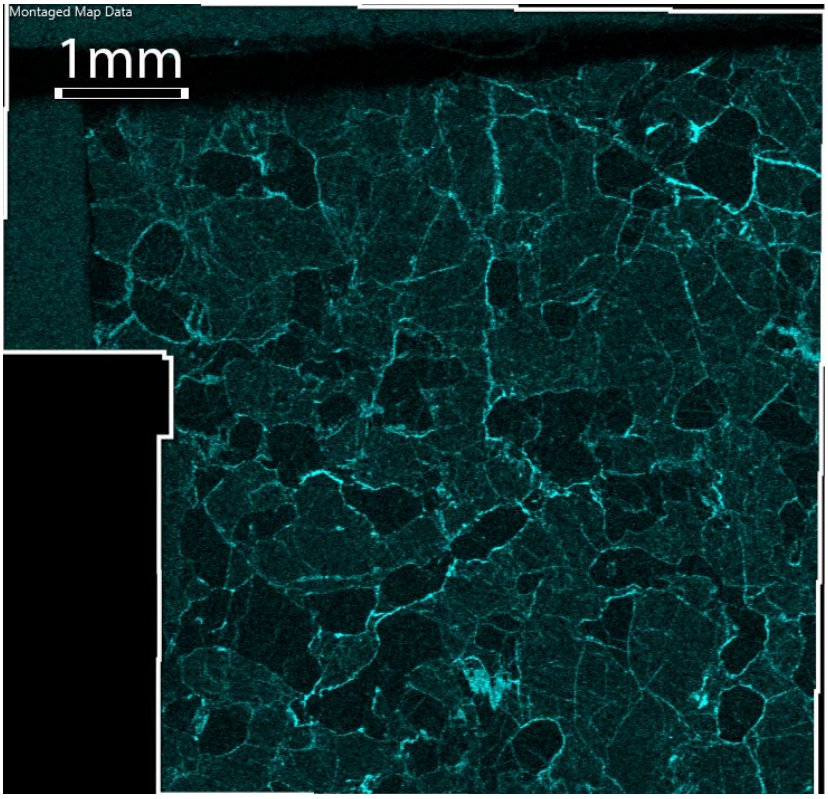

Figure 38 - SD2-LC75 potassium EDS map highlighting the occurrence of incompatible elements along grain boundaries and fractures

To test whether host kimberlite contamination could contribute to the discrepancy, trace element data from the host kimberlite (McCallum, 1991) has been incorporated at a 1% mode in **(Fig. 39)** to assess the influence of interaction between the primary mineralogy of the sample and the host kimberlite. Kimberlites in general, State Line included, exhibit negatively sloped REE profiles with LREE values ~2-3 orders of magnitude more than primitive mantle. This incorporation of 1% kimberlite in the whole rock reconstruction is shown to reduce the LREE discrepancy by approximately 50 percent.

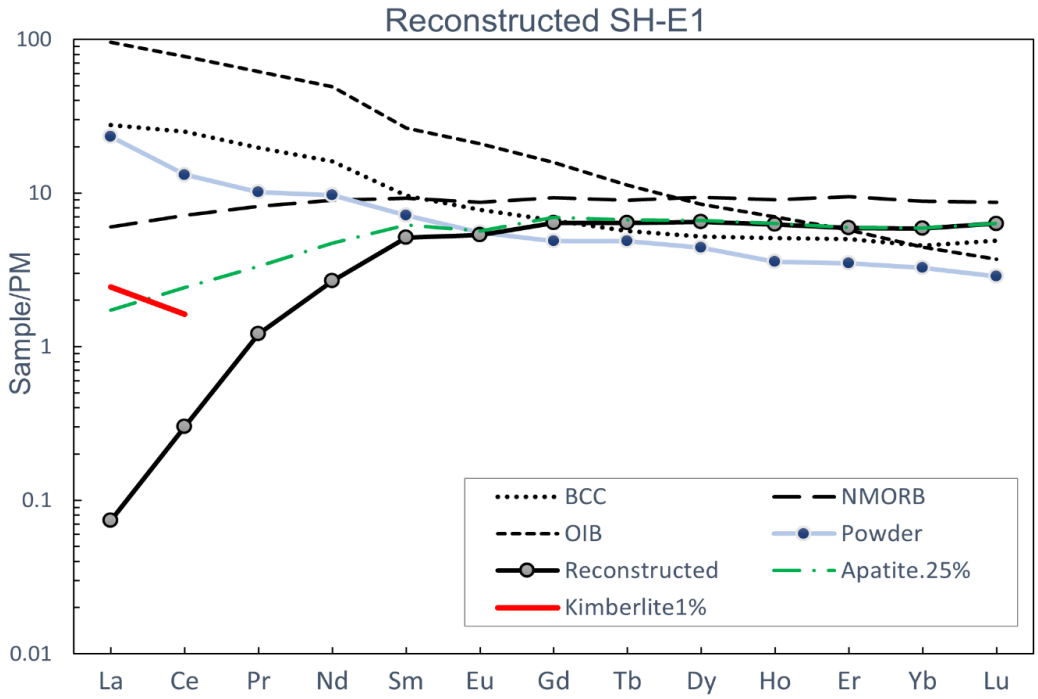

Figure 39 - SH-E1 Whole Rock reconstruction REE values with apatite and kimberlite additions to mode. Whole rock powder data from Farmer et Al. 2005. BCC- Bulk continental Crust. OIB – Ocean Island Basalt. NMORB – Normal Mid Ocean Ridge Basalt.

However, accessory minerals which concentrate REE and which are not accounted for during EDS-based modal reconstructions may also result in trace element discrepancy. Trace element data from apatite (O'Sullivan et al., 2021) has been incorporated at a 0.25% mode in **(Fig. 39)** to assess the influence of apatite as a phase in sample mineralogy. Incorporation of

0.25% apatite also reduces the LREE discrepancy by 50 percent. Apatite data sourced from granulite facies xenoliths from the Bearpaw mountains region of Montana (O'Sullivan et al., 2021); similar to the State Line region with both being Proterozoic suture zones within the North American craton.

The influence of accessory minerals is more difficult to ascertain due to small sample volumes which provide poor constraints on true mineral modes. The State Line samples analyzed were no larger than a single standard size thin section, with most samples being one-inch rounds. While we can determine whole rock reconstructions based on the mineral modes of these sections, we cannot say that these modes accurately reflect any greater volume of sample. Therefore, we cannot accurately assess the effect of the accessory minerals on whole rock trace element chemistry without further review of a larger representative volume of sample with which specific focus is made to properly analyze mineral modes with special care taken for accessory phases.

Mineral trace element partitioning

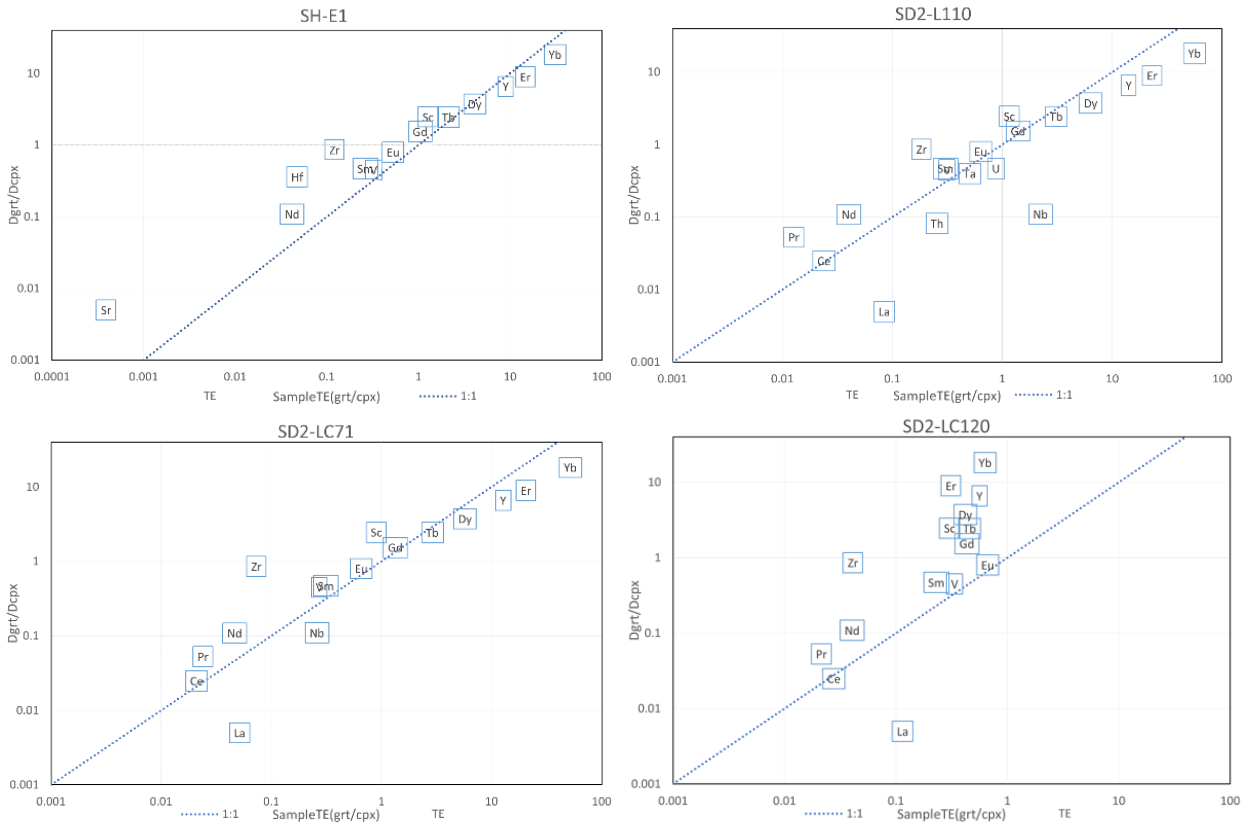

Figure 40 - Garnet/Clinopyroxene measured REE concentrations (x-axis) plotted against Garnet/Clinopyroxene distribution coefficients derived from high-pressure garnet pyroxenites (Zack et al. 1997) as a means for assessing equllibrium.

Trace element partitioning plots show measured trace element concentrations for garnet and clinopyroxene in comparison with naturally derived distribution coefficient values for garnet and clinopyroxene from similar mineralogic assemblages **(Fig. 40)**. Comparative values are derived from well equilibrated high-pressure garnet pyroxenites from Kakanui, New Zealand (Zack et al., 1997). These plots show that none of our samples are in absolute equilibrium with the comparative values. Elements that plot above the 1:1 line indicate measured garnet/clinopyroxene ratio is less than established in Kakanui samples, suggesting under-incorporation of that element into garnet. Elements that plot below the 1:1 line indicate measured garnet/clinopyroxene ratio is more than established in Kakanui samples, suggesting under-

incorporation of that element into clinopyroxene. Some natural factors which will deviate equilibrium include but are not limited to metasomatic alteration, melt/fluid interaction, and mineralogical phase transitions through P/T change. Sample SD2-LC120, for example, shows higher degrees of disequilibrium for most elements analyzed. Petrographic analysis shows that this sample has significant fracturing and secondary alteration which likely contributed to the observed disequilibrium **(Fig. 8)**.

The data used to construct these plots is derived from naturally occurring minerals. In a natural setting these partition coefficient values are defined in a system with a specific mineral assemblage and a unique bulk partition coefficient. Most of the State Line samples have garnet/clinopyroxene partitioning ratios similar to the Kakanui values, with a slight deviation towards garnet enrichment. Light rare earth elements, incompatible trace elements, and high field strength elements show higher degrees of deviation from a 1:1. This is likely due to the presence of other minerals in the State Line samples (e.g. apatite, rutile, plagioclase, orthopyroxene) that are not present in the Kakanui garnet-pyroxenites which have altered the bulk rock partition coefficients.

To qualitatively assess the influence of other minerals, we will discuss the theoretical effects of how accessory mineral phases would affect the bulk rock partition coefficient. Comparative partition coefficient values are established within Kakanui samples which are bi-mineralic. The presence of additional minerals in the State Line samples is likely a large component in the partitioning ratio discrepancies that we observe when comparing the State Line and Kakanui samples. To assess the influence of accessory minerals on bulk rock trace element partitioning we will consider the theoretical effects of the presence of three minerals: apatite,

ilmenite, and rutile. All of which are common accessory minerals within granulite facies rocks and are found in variable modes within all four of the State Line samples considered here.

Apatite occurs within the State Line samples as small, rounded crystals enclosed in plagioclase and along grain boundaries between other minerals. Phosphorous EDS maps of SD2-L110 **(Fig.41)** exhibits the abundance of apatite that exists in some of the State Line samples. Pixel counting of this image gives a calculated apatite modal percentage of approximately 1.4.

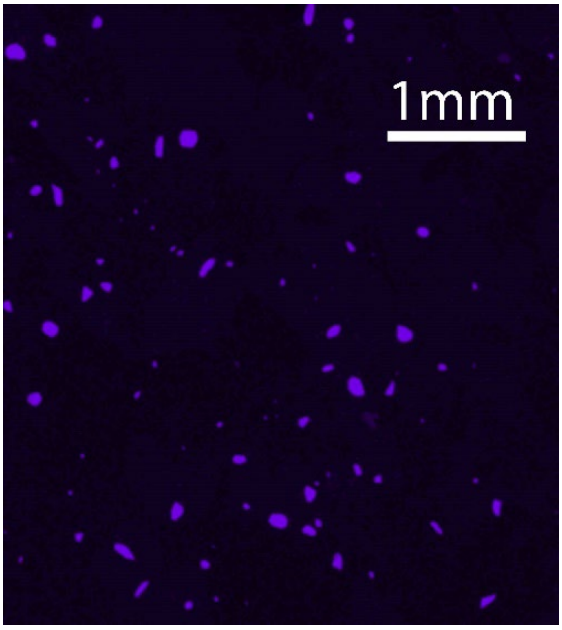

Figure 41 - SD2-L110 phosphorous EDS map showing the occurrence of apatite.

Apatite tends to incorporate high concentrations of LREE's, Th, and U (Nehring et al., 2010). We see that for sample SD2-L110 **(Fig. 41)** the lanthanum plots off the 1:1. Considering that we have up to 1.4% apatite in this sample, we can infer that this apatite is incorporating high concentrations of LREE such as lanthanum that would otherwise be partitioned into clinopyroxene. Apatite is also found in smaller volumes within SD2-LC120, and SD2-LC71; and is inferred to be imposing a similar effect on LREE partitioning though to a lesser degree than SD2-L110.

Ilmenite occurs within all State Line samples as irregularly shaped small to medium sized blebs with rounded grain boundaries and in some samples as a symplectite with pyroxene.

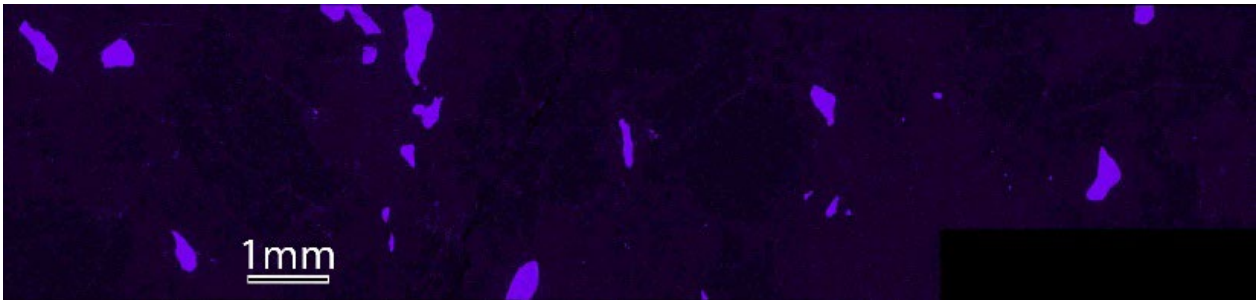

Figure 42 - SD2LC71 titanium EDS map showing the occurrence of ilmenite.

Titanium EDS maps of sample SD2-LC71 **(Fig. 42)**, highlight the ilmenite and its occurrence. Ilmenite typically has strong partitioning for the High Field Strength Elements (Hf, Zr, Ti, Nb, and Ta) as well as Sc (Nehring et al., 2010). We infer that the ilmenite within these samples is responsible for deviation of the HFSE's off the 1:1 equilibrium line, especially concerning Zr and Hf as they would otherwise be incorporated with Ti into the M1-site of clinopyroxene.

Rutile occurs within State Line samples as small to medium subrounded to rounded grains. Titanium EDS maps of sample SD2-LC120 **(Fig. 43)**, highlight the rutile grains in green. Rutile has a strong affinity for HFSE's (Hf, Zr, Ti, Nb, Ta) and a lesser affinity for other trace

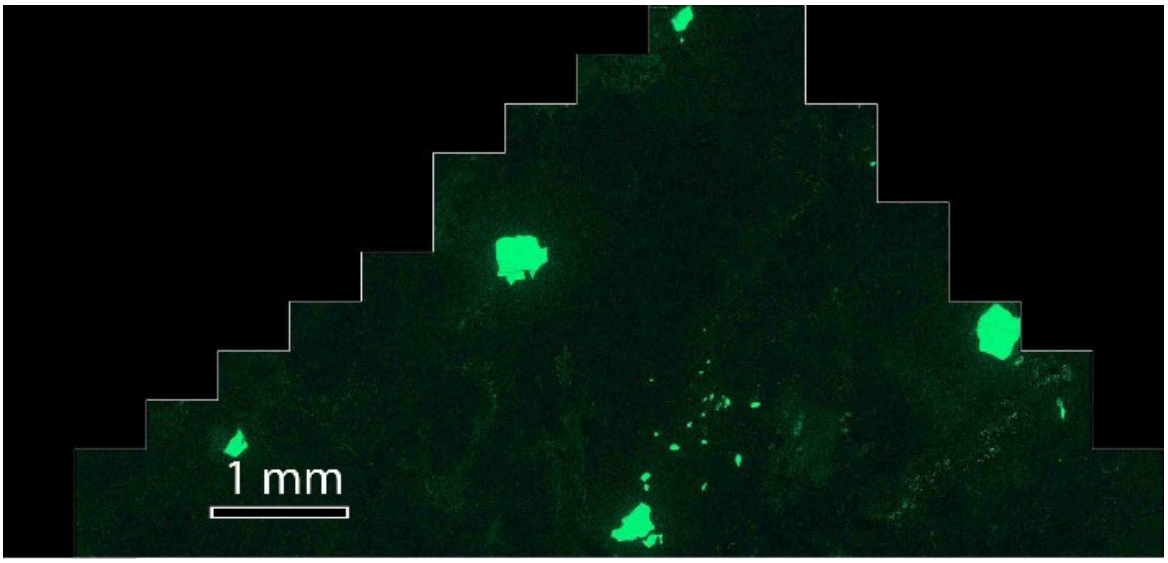

Figure 43 - SD2LC120 titanium EDS map showing the occurrence of rutile.

elements including Sb, and W (Meinhold, 2010). We infer that the rutile within these samples is responsible for deviation of the HFSE's off the 1:1 equilibrium line, particularly for samples SH-E1 and SD2-LC120 which contain rutile modes of ~1-2%.

While we do not have the ability to quantifiably assess the influence of these accessory minerals on the reported equilibria of clinopyroxene and garnet within the State Line samples; this qualitative assessment suggests that most of the disequilibrated elements are likely associated with the presence of accessory mineral phases and their effects on bulk rock partition coefficient values.

SIMS data Grain Size Analysis

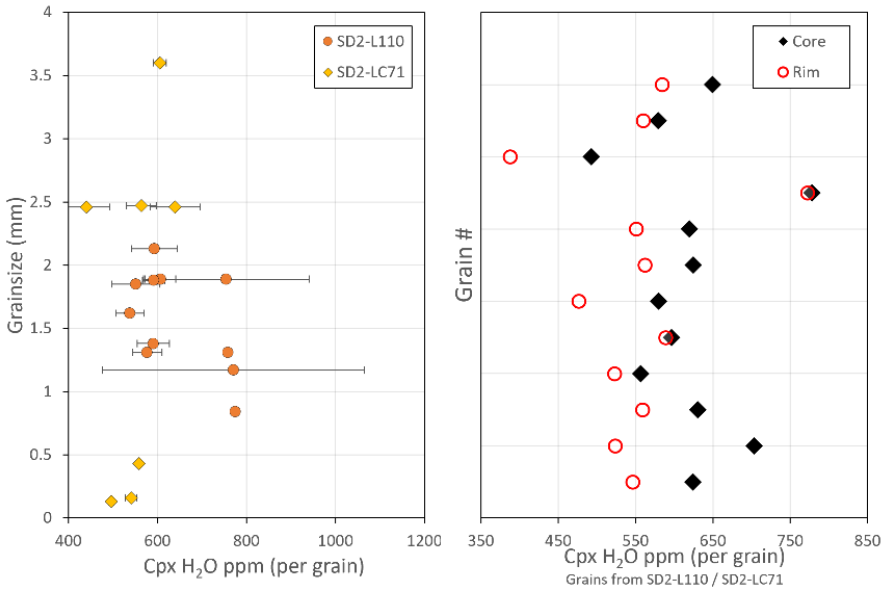

Figure 44 – State Line clinopyroxene SIMS data left) grain size right) core-rim analyses of individual grains.

Grain size analysis for clinopyroxene within State Line samples SD2-L110 and SD2-LC71 show no correlation between grain size and water content **(Fig. 44)**. Intragrain water content is shown to be higher within grain cores with respect to the grain rims **(Fig. 44)**. This

suggests water loss during eruption/exhumation along grain boundaries and supports the idea that these samples saw no metasomatic hydration at depth.

This core/rim relationship also suggests that all reconstructed whole rock water content quantities are a minimum bound on the original water content of the samples. If we assume during lower crustal residence all water had equilibrated to be homogenously distributed within any grain; the reduced hydration state of the rims suggest dehydration along grain boundaries at some point thereafter.

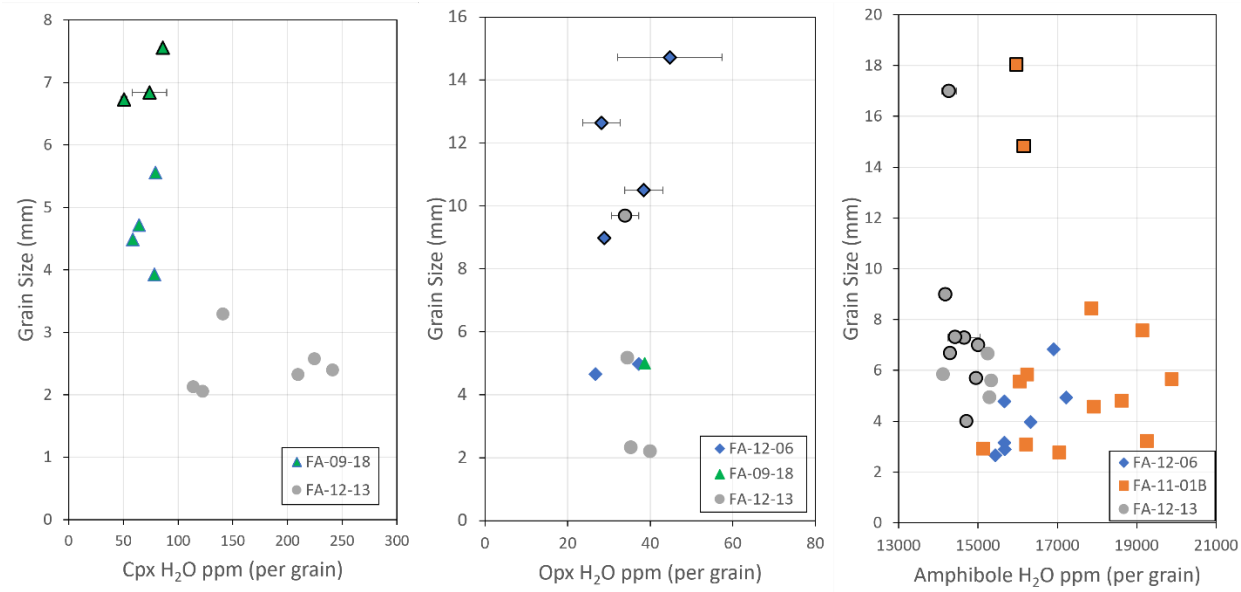

Figure 45 - Famatinia SIMS data plotted against grain size for left) clinopyroxene middle) orthopyroxene right) amphibole.

Grain size analysis of clinopyroxene, orthopyroxene, and amphibole within the Famatinia samples show little to no correlation between grain size and water content for the pyroxenes or amphibole **(Fig. 45)**.

Core-rim analysis of pyroxene within Famatinia samples **(Fig. 46)** reveals variable intragrain distribution of water. Approximately 45% of grains analyzed have more hydrous grain cores than rims with high variability across the sample set; the degree of hydration in these cores with respect to their rims range from 5 to 25 ppm. The other 55% of grains analyzed exhibit either no considerable core-rim variability or very slight hydration of grain rims with respect to cores.

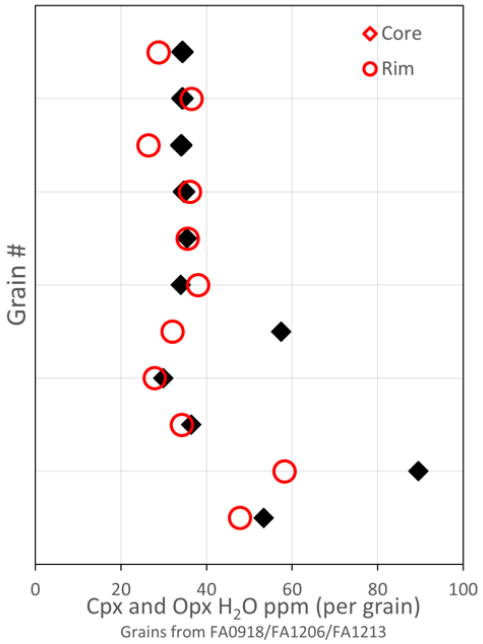

Figure 46 - Core-rim analyses of individual pyroxene grains for Famatinia samples.

SIMS data comparison with other worldwide lower crustal occurrences

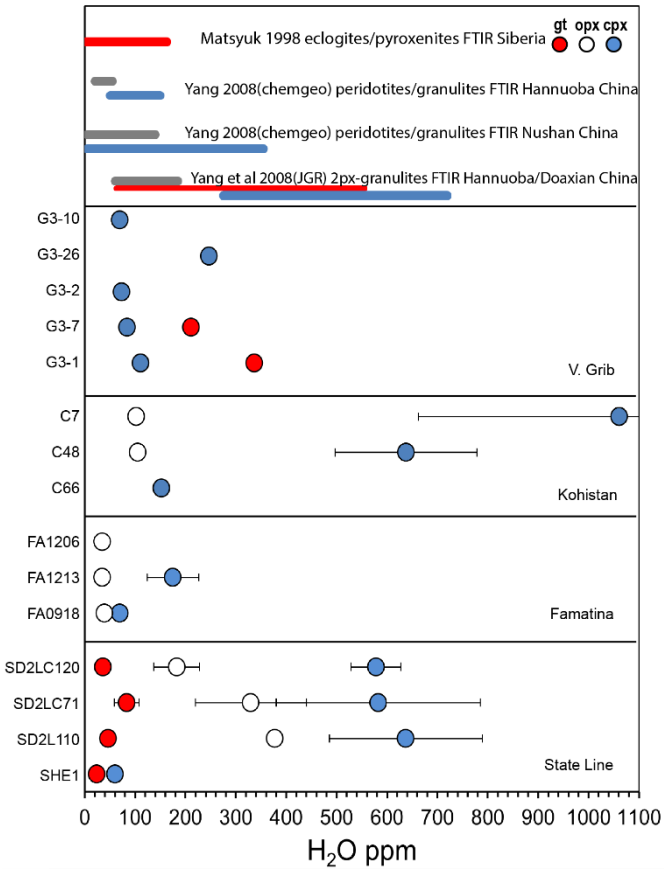

Figure 47 - Caltech style plot for average mineral H_2O derived from SIMS analyses for State Line and Famatinia samples with H_2O data from other lower crustal occurrences worldwide.

(Fig. 47) shows the range of water contents for garnet and pyroxenes from State Line, Famatinia and samples from other lower crustal occurrences around the globe including xenoliths (V. Grib kimberlite sourced eclogites (Agasheva et al., 2021), Hannuoba/Daoxian two pyroxene granulites (Yang et al., 2008a), Nushan two pyroxene peridotites (Yang et al., 2008b) and exhumed terranes (Kohistan paleo-arc gabbronorite cumulates (Urann et al., 2022), Hannuoba terrane two pyroxene granulites (Yang et al., 2008a)). State Line NAM water content is generally consistent with two pyroxene granulite xenoliths from the Hannuoba/Daoxian provinces of China (Yang et al., 2008a) though orthopyroxene values are consistently higher. When considering the relationship between State Line/Famatinia and V. Grib it is important to

note that Agasheva et al. found “no distinct or uniform correlations, indicating that a complex of various local conditions controls the incorporation of water into these minerals” (Agasheva et al., 2021). This finding is not surprising considering the reported lateral and vertical heterogeneity of lower continental crust (Rudnick and Fountain, 1995). Without a more intricate review of geochemical and petrogenetic history of the regions we cannot draw correlations between these data sets without making considerable assumptions. Additionally, it is important to note that all but one (Kohistan) of the comparative literature data shown in **(Fig. 47)** utilized Fourier-Transform Infrared Spectroscopy (FTIR) as opposed to SIMS. These two methods have different uncertainties. Additionally, FTIR generally requires large, oriented crystals and the mineral separation process removes spatial and contextual information about the sample.

There are innumerable factors to consider when comparing samples from different regions each with their own unique petrogenetic history. Here we will consider some of the differences between the State Line and Famatinia sample suites that were highlighted by our data and explore processes which may have contributed to these differences.

When considering the trends we find in the SIMS data with respect to water content in NAM it is important to highlight that these lower crustal samples suites have very different exhumation processes which brought them to the surface. The State Line samples experienced a rapid ascent to the surface, being entrained within kimberlitic host lavas, plucked from the lower crust, and promptly brought to the surface in what can be considered a lightning-fast process on geologic time scales. The Famatinia suite on the other hand experienced a long-drawn-out exhumation process as normal faulting and erosion slowly uplifted the arc terrane to its current position. The time scales between these two processes are orders of magnitude apart and this has a direct effect on the geochemical partitioning of elements, particularly Hydrogen. Hydrogen diffusivity is of

the highest elemental diffusivity rates. Considering our two sample sets have very different time scales on their exhumation, we expect that the geochemical partitioning of hydrogen will highlight these differences.

State Line samples – rapid exhumation leads to "freezing" of original water concentrations with some H loss along grain boundaries associated with rapid decompression. We see this in our grain core-rim analyses where water is shown to be lower in grain rims compared to their cores. The diffusivity of water is fast enough to lose water along grain rims during exhumation but not so fast that any significant amount of water is lost from the core of individual mineral grains. Whole rock reconstructions using water content data from mineral grain cores should closely approximate initial hydration conditions of the cumulates as they formed at depth.

Famatinia samples – slow exhumation causes re-equilibration at lower pressures with ambient fluid concentration on a large scale (whole crustal section). We find that the Famatinia samples contain more hydrous phases such as amphibole and mica which are stabilized by a higher water content than is found in the State Line samples. Famatinia samples include some textural indicators and phase relationships indicative of reaction processes which form the hydrous phases through interaction with hydrous residual liquids. FA2-11-01B, relict olivine cores surrounded by large optically continuous amphibole indicate a potential reaction between plagioclase, olivine, and a hydrous melt phase which mineralized amphibole and phlogopite. FA-12-06 exhibits similar reaction rim textures with the inclusion of orthopyroxene as an intermediate phase between olivine and amphibole. Grain analyses on the Famatinia samples show no correlation between water content and grain size **(Fig. 46)**. Additionally, we find no evidence for water content zoning within amphibole or any of the pyroxenes which is consistent with previously reported findings of no major element compositional zoning (Otamendi et al.,

2010).

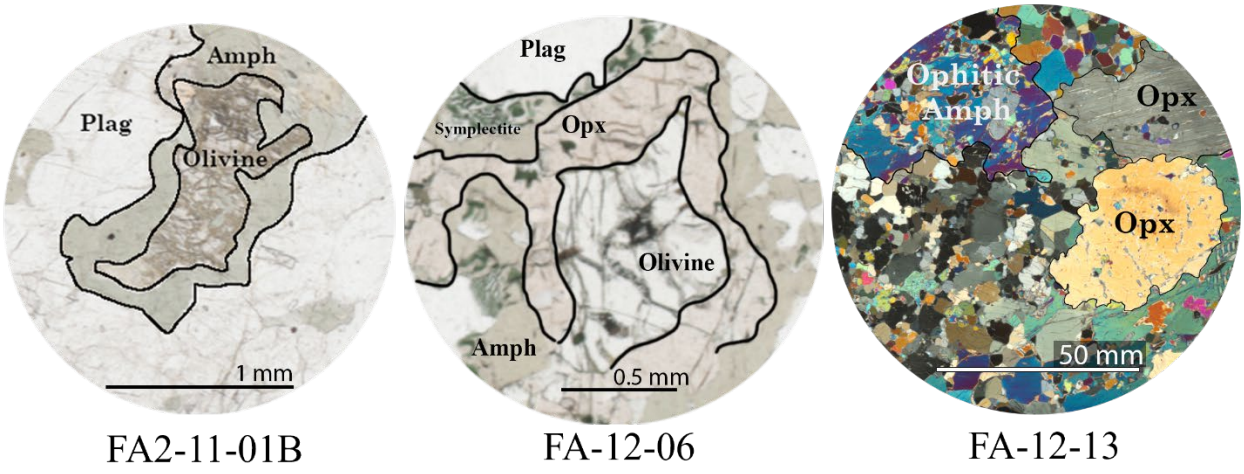

Figure 48 - Textures within Famatinia samples showing reaction textures (left,middle) and poikilitic amphibole (right).

The Famatinia samples exhibit textures and geochemical partitioning indicators which signal a significantly more complicated, dynamic, petrogenetic history compared to the State Line xenoliths. Extensive crustal residency times at gradually lesser pressures through a prolonged exhumation process has overprinted the original water concentrations; this process adding more water to the system, accommodating mineralogic reactions, and through them the repartitioning of water from NAMS to hydrous phases such as amphibole and micas.

Both sample suites exhibit reaction textures but with marked differences in mineralogic assemblages, namely the presence of hydrous phases of Famatinia suite and lack thereof in State Line suite. Reaction textures within the Famatinia samples indicate interaction with hydrous residual phases which accommodate the formation of amphibole, the primary carrier phases for H_2O in these samples **(Fig. 48)**. State Line samples also exhibit reaction textures such as coronas and symplectite within NAMs indicating dry subsolidus conditions.

Conclusion

In this study eight thin sections from two localities were studied using polarized and reflected light microscopy, EDS, SIMS, and for four samples ICPMS. Four mafic granulite samples were selected from the State Line region: SH-E1, SD2-LC120, SD2-LC71, and SD2-L110. And four amphibole bearing cumulates were selected from the Famatinia region: FA-09-18, FA-12-13, FA-09-18, FA2-11-01B.

In-situ Laser Ablation Inductively Coupled Spectrometry (LA-ICPMS) of the four State Line thin sections was utilized to quantify the abundance of 40 elements. Clinopyroxene grains exhibit a typical arched profile with relative depletion of HREE and 3 of 4 samples showing negative Eu anomalies. Coincident garnet and plagioclase are inferred to have caused HREE and Eu depletion in the clinopyroxene, respectively. Garnet grains exhibit typical HREE enrichment across all samples with SD2-LC120 showing relative depletion in HREE compared to the other samples. Orthopyroxene grains show a flat to negatively sloped trace element profile dependent on the sample with overall low content of trace elements suggesting a limited control of orthopyroxene on the trace element budget. Plagioclase grains show relatively high LREE concentrations (10-100x that of primitive mantle) with a positive Eu anomaly in all samples while HREE values fall below the detection limits of the instrument. Comparison of clinopyroxene and garnet trace element concentrations with that of experimentally derived partition coefficients for similar mineralogic assemblages suggest the State Line samples elemental distribution reflect equilibrium conditions with deviations likely associated with elemental partitioning within accessory phases.

Secondary Ion Mass Spectrometry was used to quantify water content of primary silicate mineralogy for all samples in-situ from thin-sections with mounted Suprasil glass as a reference

standard. State Line samples showed average mineral H_2O concentrations (ppm) as follows; Garnet 24 to 84, Orthopyroxene 182 to 377, and Clinopyroxene 578 to 637 with sample SH-E1 an outlier at 60 ppm. Famatinia samples showed average mineral H_2O concentrations (ppm) as follows; Clinopyroxene 70 to 175, Orthopyroxene 35 to 39, and Amphibole 14644 to 17096. Comparisons with other published NAM H_2O values reveal similarities between the hydration state of NAMS from the State Line region and 2-pyroxene granulites from Hannuoba and Doaxian region of China as well as cumulate gabbronorites from the Kohistan paleo-arc terrane within Pakistan, particularly concerning the hydration state of clinopyroxene. These findings highlight the importance of clinopyroxene as a carrier phase for water within the deep lower crust.

Whole rock reconstructions were calculated using mineral modes determined from pixel counting coupled with data from SIMS and LA-ICPMS analyses. Dispersive X-ray spectroscopy (EDS) was utilized on carbon or gold coated thin sections to produce elemental distribution maps of up to 13 elements. Pixel counting with Adobe Photoshop was performed to quantify the mineral modes using EDS maps. Whole rock reconstructions revealed a positive correlation between whole rock H_2O and trace element concentrations across the State Line sample set, suggesting a connected petrogenetic history or lineage from a shared magma source. Additionally, analysis of whole rock reconstructions for State Line sample trace element chemistry suggest LREEs are concentrated within accessory minerals phases such as apatite as well as host lava contaminant zones along grain boundaries and fractures.

Grain size analyses and core-rim analyses were used to assess correlations between grain size, water content of individual grains, and intra-grain water distribution. Grain size analyses reveal no correlation between grain size and water content of minerals for either the State Line or

Famatinia samples. Core-rim analyses find no consistent intra-grain variation within the Famatinia minerals though State Line samples exhibit comparatively hydrous grain cores with respect their rims, suggestive of water loss across phase boundaries during exhumation through entrainment within kimberlitic host lavas and subsequent eruption. These findings indicate that the State Line samples preserve original/primary trace element chemistry within grain cores and water content which act as a minimum bound on the original hydration state. Famatinia samples are inferred to have re-equilibrated at lower pressures with ambient fluid concentration on a large scale (whole crustal section) and formation of amphibole as a secondary hydrous phase through interaction with residual hydrous melts.

Future Research

The data collected in this study may facilitate future research into the physical effects of water content within lower crust mineral assemblages with respect to long-term stability, rheology, and tectonic implications through geophysical modelling. Accurately defining the water content of lower crustal rocks has numerous challenges, though the methodology utilized in this study and assessment of the State Line samples regarding equilibrium conditions and water retention suggest that the data outlined here provides an accurate quantification of the hydration state of an arc derived lower crustal fractional crystallization sequence.

To continue research in this study, it would be useful quantify the trace element composition of accessory phases in the State Line samples, ideally using a larger sample volume, providing better constraints on true trace element profile of whole rock. Whole rock reconstructions as were conducted provide a means to assess general chemical relationships between the State Line samples though incorporation of the various accessory minerals would permit a much more comprehensive analysis. Inclusion of accessory mineral data provides the

basis for a quantitative assessment of the chemical influence of grain boundary alteration associated with the kimberlitic host material, and a means to quantify the chemical composition of the magmas from which these samples fractionated from, shedding light on the chemical behavior of magmas within Proterozoic arc systems.

Table 8 – SIMS data for all samples analyzed values reported in ppm.

		SHE1	SD2L10	SD2LC71	SD2LC120	FA1206	FA1101B	FA0918	FA1213
Garnet	min	19	69	99	70				
	max	67	102	230	104				
	avg	42	77	139	83				
	1SD	13	9.9	41	15				
	n - grain	6	2	9	7				
	n - spot	11	10	19	7				
Cpx	min	62	476	345	634			48	114
	max	96	1225	1178	835			90	241
	avg	75	637	583	726			70	175
	1σ	9.8	152	202	62			14.6	51.1
	n - grain	11	9	11	3			7	6
	n - spot	20	44	27	9			10	6
Opx	min		372	249	132	24		39	26
	max		380	647	322	57		39	41
	avg		377	330	233	35			35
	1σ		4.4	110	56	9			3.4
	n - grain		2	6	3	6		1	8
	n - spot		3	14	7	11		1	19
Plagioclase	min		9.77	32.04	31.2	4.5	1.29	11.58	17.9
	max		38.76	79.37	42.1	7.05	3.31	21.18	17.9
	avg		28.08	55.70	39.1	6.16	1.94	14.7	
	1σ		8.83	23.66	4.1	0.98	0.8	3.32	
	n - grain			2	5	4	4	6	1
	n - spot			2	5	4	4	6	1
Amphibole	min					15439	15132		13964
	max					17224	19877		15329
	avg					16129	17096		14644
	1σ					649	1420		414
	n - grain					7	13		13
	n - spot					7	16		24
Olivine	min					5.2	70		
	max					7.1	70		
	avg					5.8			
	1σ					0.6			
	n - grain					5	1		
	n - spot					10	1		

References

Agasheva, E.V., Kolesnichenko, M.V., Malygina, E.V., Agashev, A.M., Zedgenizov, D.A., 2021. Origin of Water in Mantle Eclogites from the V. Grib Kimberlite Pipe, NW Russia. Lithosphere 2021, 7866657. https://doi.org/10.2113/2021/7866657

Arndt, N., 2013. Formation and Evolution of the Continental Crust. GeochemPersp 2, 405–533. https://doi.org/10.7185/geochempersp.2.3

Astini, R.A., Dávila, F.M., 2004. Ordovician back arc foreland and Ocloyic thrust belt development on the western Gondwana margin as a response to Precordillera terrane accretion. Tectonics 23. https://doi.org/10.1029/2003TC001620

Aubaud, C., Withers, A.C., Hirschmann, M.M., Guan, Y., Leshin, L.A., Mackwell, S.J., Bell, D.R., 2007. Intercalibration of FTIR and SIMS for hydrogen measurements in glasses and nominally anhydrous minerals. American Mineralogist 92, 811–828. https://doi.org/10.2138/am.2007.2248

Bickford, M.E., Van, W.R., Zietz, I., 1986. Proterozoic history of the midcontinent region of North America. Geol 14, 492. https://doi.org/10.1130/0091-7613(1986)14<492:PHOTMR>2.0.CO;2

Bradley, S.D., McCallum, M.E., 1984. Granulite Facies and Related Xenoliths from Colorado-Wyoming Kimberlite, in: Kornprobst, J. (Ed.), Developments in Petrology, Kimberlites. Elsevier, pp. 205–217. https://doi.org/10.1016/B978-0-444-42274-3.50023-8

Cavosie, A., Selverstone, J., 2003. Early Proterozoic oceanic crust in the northern Colorado Front Range: Implications for crustal growth and initiation of basement faults: PROTEROZOIC OCEANIC CRUST IN COLORADO. Tectonics 22. https://doi.org/10.1029/2001TC001325

Cawood, P.A., 2005. Terra Australis Orogen: Rodinia breakup and development of the Pacific and Iapetus margins of Gondwana during the Neoproterozoic and Paleozoic. Earth-Science Reviews 69, 249–279. https://doi.org/10.1016/j.earscirev.2004.09.001

Chin, E.J., Curran, S.T., Farmer, G.L., 2020. Squeezing Water From a Stone: H2O In Nominally Anhydrous Minerals From Granulite Xenoliths and Deep, Hydrous Fractional Crystallization. Journal of Geophysical Research: Solid Earth 125. https://doi.org/10.1029/2020JB020416

Chin, E.J., Shimizu, K., Bybee, G.M., Erdman, M.E., 2018. On the development of the calc-alkaline and tholeiitic magma series: A deep crustal cumulate perspective. Earth and Planetary Science Letters 482, 277–287. https://doi.org/10.1016/j.epsl.2017.11.016

Chin, E.J., Soustelle, V., Hirth, G., Saal, A.E., Kruckenberg, S.C., Eiler, J.M., 2016. Microstructural and geochemical constraints on the evolution of deep arc lithosphere. Geochemistry, Geophysics, Geosystems 17, 2497–2521. https://doi.org/10.1002/2015GC006156

Collins, W.J., Murphy, J.B., Johnson, T.E., Huang, H.-Q., 2020. Critical role of water in the formation of continental crust. Nat. Geosci. 13, 331–338. https://doi.org/10.1038/s41561-020-0573-6

Collo, G., Astini, R.A., Cawood, P.A., Buchan, C., Pimentel, M., 2009. U–Pb detrital zircon ages and Sm–Nd isotopic features in low-grade metasedimentary rocks of the Famatina belt: implications for late Neoproterozoic–early Palaeozoic evolution of the proto-Andean margin of Gondwana. Journal of the Geological Society 166, 303–319. https://doi.org/10.1144/0016-76492008-051

Condie, K.C., 1999. Mafic crustal xenoliths and the origin of the lower continental crust. Lithos 46, 95–101. https://doi.org/10.1016/S0024-4937(98)00056-5

Davidson, J., Turner, S., Handley, H., Macpherson, C., Dosseto, A., 2007. Amphibole "sponge" in arc crust? Geology 35, 787–790. https://doi.org/10.1130/G23637A.1

Defant, M.J., Drummond, M.S., 1990. Derivation of some modern arc magmas by melting of young subducted lithosphere. Nature 347, 662–665. https://doi.org/10.1038/347662a0

Dickinson, W.R., Snyder, W.S., 1978. Plate tectonics of the Laramide orogeny. https://doi.org/10.1130/MEM151-p355

Ducea, M.N., 2002. Constraints on the bulk composition and root foundering rates of continental arcs: A California arc perspective: Arc Composition and Foundering Rates. J. Geophys. Res. 107, ECV 15-1-ECV 15-13. https://doi.org/10.1029/2001JB000643

Ducea, M.N., Bergantz, G.W., Crowley, J.L., Otamendi, J., 2017. Ultrafast magmatic buildup and diversification to produce continental crust during subduction. Geology 45, 235–238. https://doi.org/10.1130/G38726.1

Ducea, M.N., Otamendi, J.E., Bergantz, G., Stair, K.M., Valencia, V.A., Gehrels, G.E., 2010. Timing constraints on building an intermediate plutonic arc crustal section: U- Pb zircon geochronology of the Sierra Valle Fértil-La Huerta, Famatinian arc, Argentina: Geochronology of the Famatinian Arc. Tectonics 29, n/a-n/a. https://doi.org/10.1029/2009TC002615

Eggler, D.H., McCallum, M.E., Kirkley, M.B., 1987. Kimberlite-transported nodules from Colorado-Wyoming; A record of enrichment of shallow portions of an infertile lithosphere. Geological Society of America Special Paper 215, 77–90.

Farmer, G.L., Bowring, S.A., Williams, M.L., Christensen, N.I., Matzel, J.P., Stevens, L., 2005. Contrasting Lower Crustal Evolution Across an Archean: Proterozoic Suture: Physical, Chemical and Geochronologic Studies of Lower Crustal Xenoliths in Southern Wyoming and Northern Colorado, in: The Rocky Mountain Region: An Evolving Lithosphere. American Geophysical Union (AGU), pp. 139–162. https://doi.org/10.1029/154GM11

Farmer, G.L., Fritz, D.E., Glazner, A.F., 2020. Identifying Metasomatized Continental Lithospheric Mantle Involvement in Cenozoic Magmatism From Ta/Th Values, Southwestern

North America. Geochemistry, Geophysics, Geosystems 21. https://doi.org/10.1029/2019GC008499

Gallien, F., Mogessie, A., Hauzenberger, C.A., Bjerg, E., Delpino, S., Castro De Machuca, B., 2012. On the origin of multi-layer coronas between olivine and plagioclase at the gabbro–granulite transition, Valle Fértil–La Huerta Ranges, San Juan Province, Argentina. Journal of Metamorphic Geology 30, 281–302. https://doi.org/10.1111/j.1525-1314.2011.00967.x

H. S. Yoder Jr., Kushiro, J., 1969. Melting of a hydrous phase: phlogopite. American Journal of Science 267, 558–582.

Hirth, G., Kohlstedt, D.L., 1995. Experimental constraints on the dynamics of the partially molten upper mantle: Deformation in the diffusion creep regime. J. Geophys. Res. 100, 1981–2001. https://doi.org/10.1029/94JB02128

Humphreys, E., Hessler, E., Dueker, K., Farmer, G.L., Erslev, E., Atwater, T., 2003. How Laramide-Age Hydration of North American Lithosphere by the Farallon Slab Controlled Subsequent Activity in the Western United States. International Geology Review 45, 575–595. https://doi.org/10.2747/0020-6814.45.7.575

Ingrin, J., Blanchard, M., 2006. Diffusion of Hydrogen in Minerals. Reviews in Mineralogy and Geochemistry 62, 291–320. https://doi.org/10.2138/rmg.2006.62.13

Jagoutz, O.E., 2010. Construction of the granitoid crust of an island arc. Part II: a quantitative petrogenetic model. Contrib Mineral Petrol 160, 359–381. https://doi.org/10.1007/s00410-009-0482-6

Jones, C.H., Mahan, K.H., Butcher, L.A., Levandowski, W.B., Farmer, G.L., 2015. Continental uplift through crustal hydration. Geology 43, 355–358. https://doi.org/10.1130/G36509.1

Keller, G.R., Karlstrom, K.E., Williams, M.L., Miller, K.C., Andronicos, C., Levander, A.R., Snelson, C.M., Prodehl, C., 2005. The Dynamic Nature of the Continental Crust-Mantle Boundary: Crustal Evolution in the Southern Rocky Mountain Region as an Example, in: The Rocky Mountain Region: An Evolving Lithosphere. American Geophysical Union (AGU), pp. 403–420. https://doi.org/10.1029/154GM30

Lange, R.A., Carmichael, I.S.E., Hall, C.M., 2000. 40Ar/39Ar chronology of the Leucite Hills, Wyoming: eruption rates, erosion rates, and an evolving temperature structure of the underlying mantle. Earth and Planetary Science Letters 174, 329–340. https://doi.org/10.1016/S0012-821X(99)00267-8

Lee, C.-T.A., 2014. Physics and Chemistry of Deep Continental Crust Recycling, in: Treatise on Geochemistry. Elsevier, pp. 423–456. https://doi.org/10.1016/B978-0-08-095975-7.00314-4

Lee, C.-T.A., Anderson, D.L., 2015. Continental crust formation at arcs, the arclogite "delamination" cycle, and one origin for fertile melting anomalies in the mantle. Sci. Bull. 60, 1141–1156. https://doi.org/10.1007/s11434-015-0828-6

Lee, C.-T.A., Cheng, X., Horodyskyj, U., 2006. The development and refinement of continental arcs by primary basaltic magmatism, garnet pyroxenite accumulation, basaltic recharge and delamination: insights from the Sierra Nevada, California. Contrib Mineral Petrol 151, 222–242. https://doi.org/10.1007/s00410-005-0056-1

Li, Z.-X.A., Lee, C.-T.A., Peslier, A.H., Lenardic, A., Mackwell, S.J., 2008. Water contents in mantle xenoliths from the Colorado Plateau and vicinity: Implications for the mantle rheology and hydration-induced thinning of continental lithosphere. J. Geophys. Res. 113, B09210. https://doi.org/10.1029/2007JB005540

McCallum, M.E., 1991. The Sloan 1 and 2 Kimberlite Complex Near the Southern Boundary of the State Line District of the Colorado-Wyoming Kimberlite Province 229–250.

McLelland, J.M., Whitney, P.R., 1980. A generalized garnet-forming reaction for metaigneous rocks in the Adirondacks. Contr. Mineral. and Petrol. 72, 111–122. https://doi.org/10.1007/BF00399472

Meinhold, G., 2010. Rutile and its applications in earth sciences. Earth-Science Reviews 102, 1–28. https://doi.org/10.1016/j.earscirev.2010.06.001

Michael, P., 1995. Regionally distinctive sources of depleted MORB: Evidence from trace elements and H2O. Earth and Planetary Science Letters 131, 301–320. https://doi.org/10.1016/0012-821X(95)00023-6

Michard, A., 1989. Rare earth element systematics in hydrothermal fluids. Geochimica et Cosmochimica Acta 53, 745–750. https://doi.org/10.1016/0016-7037(89)90017-3

Mosenfelder, J.L., Le Voyer, M., Rossman, G.R., Guan, Y., Bell, D.R., Asimow, P.D., Eiler, J.M., 2011. Analysis of hydrogen in olivine by SIMS: Evaluation of standards and protocol. American Mineralogist 96, 1725–1741. https://doi.org/10.2138/am.2011.3810

Mosenfelder, J.L., Rossman, G.R., 2013a. Analysis of hydrogen and fluorine in pyroxenes: II. Clinopyroxene. American Mineralogist 98, 1042–1054. https://doi.org/10.2138/am.2013.4413

Mosenfelder, J.L., Rossman, G.R., 2013b. Analysis of hydrogen and fluorine in pyroxenes: I. Orthopyroxene. American Mineralogist 98, 1026–1041. https://doi.org/10.2138/am.2013.4291

Müntener, O., Ulmer, P., 2006. Experimentally derived high-pressure cumulates from hydrous arc magmas and consequences for the seismic velocity structure of lower arc crust. Geophysical Research Letters 33. https://doi.org/10.1029/2006GL027629

Nehring, F., Foley, S.F., Hölttä, P., 2010. Trace element partitioning in the granulite facies. Contrib Mineral Petrol 159, 493–519. https://doi.org/10.1007/s00410-009-0437-y

O'Sullivan, G.J., Thakurdin, Y., Bolhar, R., Horváth, P., Hoare, B.C., Collerson, K.D., 2021. The Great Falls Tectonic Zone after the assembly of Laurentia: evidence for long-term tectonic stability from xenolith apatite. Lithos 384–385, 105977. https://doi.org/10.1016/j.lithos.2021.105977

Otamendi, J.E., Cristofolini, E., Tibaldi, A.M., Quevedo, F.I., Baliani, I., 2010. Petrology of mafic and ultramafic layered rocks from the Jaboncillo Valley, Sierra de Valle Fértil, Argentina: Implications for the evolution of magmas in the lower crust of the Famatinian arc. Journal of South American Earth Sciences 29, 685–704. https://doi.org/10.1016/j.jsames.2009.11.001

Otamendi, J.E., Vujovich, G.I., de la Rosa, J.D., Tibaldi, A.M., Castro, A., Martino, R.D., Pinotti, L.P., 2009. Geology and petrology of a deep crustal zone from the Famatinian paleo-arc, Sierras de Valle Fértil and La Huerta, San Juan, Argentina. Journal of South American Earth Sciences, Magmatism, Crustal Evolution, and Metallogenesis of Carajás and adjacent provinces 27, 258–279. https://doi.org/10.1016/j.jsames.2008.11.007

Pankhurst, R.J., Rapela, C.W., Saavedra, J., Baldo, E., Dahlquist, J., Pascua, I., Fanning, C.M., 1998. The Famatinian magmatic arc in the central Sierras Pampeanas: an Early to Mid-Ordovician continental arc on the Gondwana margin. Geological Society, London, Special Publications 142, 343–367. https://doi.org/10.1144/GSL.SP.1998.142.01.17

Plank, T., Kelley, K.A., Zimmer, M.M., Hauri, E.H., Wallace, P.J., 2013. Why do mafic arc magmas contain 4wt% water on average? Earth and Planetary Science Letters 364, 168–179. https://doi.org/10.1016/j.epsl.2012.11.044

Rapp, R.P., Shimizu, N., Norman, M.D., 2003. Growth of early continental crust by partial melting of eclogite. Nature 425, 605–609. https://doi.org/10.1038/nature02031

Rudnick, R.L., Fountain, D.M., 1995. Nature and composition of the continental crust: A lower crustal perspective. Reviews of Geophysics 33, 267–309. https://doi.org/10.1029/95RG01302

Scholl, D.W., Vallier, T.L., Stevenson, A.J., 1986. Terrane accretion, production, and continental growth: A perspective based on the origin and tectonic fate of the Aleutian–Bering Sea region. Geol 14, 43. https://doi.org/10.1130/0091-7613(1986)14<43:TAPACG>2.0.CO;2

Sobolev, A.V., Chaussidon, M., 1996. H2O concentrations in primary melts from supra-subduction zones and mid-ocean ridges: Implications for H2O storage and recycling in the mantle. Earth and Planetary Science Letters 137, 45–55. https://doi.org/10.1016/0012-821X(95)00203-O

Tibaldi, A.M., Otamendi, J.E., Cristofolini, E.A., Baliani, I., Walker, B.A., Bergantz, G.W., 2013. Reconstruction of the Early Ordovician Famatinian arc through thermobarometry in lower and middle crustal exposures, Sierra de Valle Fértil, Argentina. Tectonophysics 589, 151–166. https://doi.org/10.1016/j.tecto.2012.12.032

Urann, B.M., Le Roux, V., Jagoutz, O., Müntener, O., Behn, M.D., Chin, E.J., 2022. High water content of arc magmas recorded in cumulates from subduction zone lower crust. Nat. Geosci. 15, 501–508. https://doi.org/10.1038/s41561-022-00947-w

Walker, B.A., Jr, Bergantz, G.W., Otamendi, J.E., Ducea, M.N., Cristofolini, E.A., 2015. A MASH Zone Revealed: the Mafic Complex of the Sierra Valle Fértil. Journal of Petrology 56, 1863–1896. https://doi.org/10.1093/petrology/egv057

Whitmeyer, S.J., Karlstrom, K.E., 2007. Tectonic model for the Proterozoic growth of North America 40.

Yang, X.-Z., Deloule, E., Xia, Q.-K., Fan, Q.-C., Feng, M., 2008a. Water contrast between Precambrian and Phanerozoic continental lower crust in eastern China. Journal of Geophysical Research: Solid Earth 113. https://doi.org/10.1029/2007JB005541

Yang, X.-Z., Xia, Q.-K., Deloule, E., Dallai, L., Fan, Q.-C., Feng, M., 2008b. Water in minerals of the continental lithospheric mantle and overlying lower crust: A comparative study of peridotite and granulite xenoliths from the North China Craton. Chemical Geology 256, 33–45. https://doi.org/10.1016/j.chemgeo.2008.07.020

Zack, T., Foley, S.F., Jenner, G.A., 1997. A consistent partition coefficient set for clinopyroxéne, amphibole and garnet from laser ablation microprobe analysis of garnet pyroxenites from Kakanui, New Zealand. Neues Jahrbuch fur Mineralogie, Abhandlungen 172, 23–41. https://doi.org/10.1127/njma/172/1997/23